International Journal of Nanomedicine

Dovepress
Taylor & Francis Group

Open Access Full Text Article

ORIGINAL RESEARCH

Ginger-Derived Exosome-Like Nanoparticles Loaded With Indocyanine Green Enhances Phototherapy Efficacy for Breast Cancer

Zhaoming Guo[1,2,*], Guqing Li[2,*], Lanjun Shen[2], Jiawei Pan[2], Danni Dou[2], Yuwei Gong[2], Wanwan Shi[2], Yuhua Sun[2], Yi Zhang[2], Kun Ma[2], Changhao Cui[2], Wenxin Li[3,4], Qiang Liu[5], Xudong Zhu[1,4,6]

[1]Department of General Surgery, Cancer Hospital of Dalian University of Technology, Cancer Hospital of China Medical University, Liaoning Cancer Hospital & Institute, Shenyang, Liaoning, 110042, People's Republic of China; [2]School of Chemical Engineering, Marine and Life Sciences, Dalian University of Technology, Panjin, Liaoning, 124221, People's Republic of China; [3]The second Department of Hepatopancreatobiliary Surgery, Cancer Hospital of Dalian University of Technology, Cancer Hospital of China Medical University, Liaoning Cancer Hospital & Institute, Shenyang, Liaoning, 110042, People's Republic of China; [4]Liaoning Provincial Key Laboratory of Precision Medicine for Malignant Tumors, Shenyang, Liaoning, 110042, People's Republic of China; [5]Faculty of Medicine, Dalian University of Technology, Dalian, Liaoning, 116024, People's Republic of China; [6]Department of Oncology, Shengjing Hospital of China Medical University, Shenyang, Liaoning, 110004, People's Republic of China

*These authors contributed equally to this work

Correspondence: Xudong Zhu, Department of General Surgery, Cancer Hospital of Dalian University of Technology, Cancer Hospital of China Medical University, Liaoning Cancer Hospital & Institute, Shenyang, Liaoning, 110042, People's Republic of China, Tel +86 13354204706, Email xdzhu@cmu.edu.cn; XudongZhu@uky.edu; Qiang Liu, Faculty of Medicine, Dalian University of Technology, Dalian, Liaoning, 116024, People's Republic of China, Email andyliu_1844@dlut.edu.cn

---

Purpose: Phototherapy has remarkable advantages in cancer treatment, owing to its high efficiency and minimal invasiveness. Indocyanine green (ICG) plays an important role in photo-mediated therapy. However, it has several disadvantages such as poor stability in aqueous solutions, easy aggregation of molecules, and short plasma half-life. This study aimed to develop an efficient nanoplatform to enhance the effects of photo-mediated therapy.

Methods: We developed a novel bio-nanoplatform by integrating edible ginger-derived exosome-like nanoparticles (GDNPs) and the photosensitizer, ICG (GDNPs@ICG). GDNPs were isolated from ginger juice and loaded with ICG by co-incubation. The size distribution, zeta potential, morphology, total lipid content, and drug release behavior of the GDNPs@ICG were characterized. The photothermal performance, cellular uptake and distribution, cytotoxicity, anti-tumor effects, and mechanism of action of GDNPs@ICG were investigated both in vitro and in vivo.

Results: GDNPs@ICG were taken up by tumor cells via a lipid-dependent pathway. When irradiated by an 808 nm NIR laser, GDNPs@ICG generated high levels of ROS, MDA, and local hyperthermia within the tumor, which caused lipid peroxidation and ER stress, thus enhancing the photo-mediated breast tumor therapy effect. Furthermore, in vivo studies demonstrated that engineered GDNPs@ICG significantly inhibited breast tumor growth and presented limited toxicity. Moreover, by detecting the expression of CD31, N-cadherin, IL-6, IFN-γ, CD8, p16, p21, and p53 in tumor tissues, we found that GDNPs@ICG substantially reduced angiogenesis, inhibited metastasis, activated the anti-tumor immune response, and promoted cell senescence in breast tumor.

Conclusion: Our study demonstrated that the novel bio-nanoplatform GDNPs@ICG enhanced the photo-mediated therapeutic effect in breast tumor. GDNPs@ICG could be an alternative for precise and efficient anti-tumor phototherapy.

Keywords: ginger-derived exosome-like nanoparticles, phototherapy, indocyanine green, lipid peroxidation, ER stress

---

Introduction

Phototherapy, including photodynamic therapy (PDT) and photothermal therapy (PTT), has been widely studied because of its advantages, such as safety, non-drug resistance, good therapeutic effects, and minimal invasiveness.[1–4] PDT is based on photosensitizers, and PTT is based on photothermal effects. Both PDT and PTT have the potential to induce

Received: 24 July 2024
Accepted: 15 January 2025
Published: 30 January 2025

immunogenic cell death (ICD) of tumor cells as well as the release of damage-associated molecular patterns (DAMPs) and tumor-associated antigens (TAAs), which can activate anti-tumor immune responses and assist in tumor therapy.[5–8] Indocyanine green (ICG) is the only FDA-approved near-infrared (NIR) fluorescent dye for clinical use in human, and it plays an important role in PDT, PTT, and photoacoustic therapy.[9–12] However, ICG has several disadvantages, such as poor stability in aqueous solutions, tendency to easily aggregate, and short plasma half-life. All these weaknesses limit its wider application.[13–15] In addition, inadequate tumor targeting by photosensitizers and insufficient tissue penetration of light seriously affect the outcomes of photo-mediated therapy. Thus, the development of orchestrated nanoplatforms to improve the bioavailability and tumor-targeting ability of ICG is a promising avenue for efficient phototherapy.

Recently, exosomes have attracted attention as nanocarriers because of their circulatory stability, biocompatibility, low immunogenicity, and ability to cross various physiological barriers.[16–19] It has been found that not only animal cells but also a variety of plant cells can produce exosome-like nanoparticles, which play an important role in intercellular communication and in maintaining homeostasis of the internal environment of organisms.[20–22] In addition, plant-derived exosome-like nanoparticles are mass-producible, economical, and benign, with low immunogenicity.[23,24] A recent study showed that exosome-like nanoparticles derived from ginger are rich in lipids, consisting of high levels of phosphatidic acid, digalactosyl, diacylglycerol, and monogalactosyldiacylglycerol.[25] The presence of the active ingredient 6-shogaol in ginger exosome-like nanovesicles has been validated by high-performance liquid chromatography-tandem mass spectrometry (HPLC/MS) and thin-layer chromatography analysis.[25,26] Numerous in vitro and in vivo investigations have demonstrated that the toxicity of 6-shogaol to normal cells or tissues is minimal, but it is effective in killing tumor cells.[27] Furthermore, 6-shogaol significantly upregulated the expression and phosphorylation of endoplasmic reticulum (ER) stress markers,[28–31] such as GRP78/Bip, eIF-2α, PERK, and CHOP,[32,33] effectively inhibiting the growth and survival of tumor cells. Hence, ginger-derived exosome-like nanoparticles (GDNPs) are being explored as next-generation biotherapeutic and nano-delivery carriers to address current clinical needs and challenges.

Tumor cells undergo increased lipid uptake and accumulation to adapt to nutrient-poor and hypoxic tumor microenvironment.[34–36] Therefore, taking advantage of the lipid metabolism preferences of tumor cells, we utilized GDNPs, which were rich in lipids and easily up-taken by tumor cells, as a new nanocarrier to load ICG, then, GDNPs@ICG was built successfully. GDNPs@ICG effectively enhanced the photomediated anti-breast tumor therapy effect by inducing the generation of reactive oxygen species (ROS), lipid peroxidation, and ER stress. Furthermore, excessive ROS production and ER stress inhibited the growth and survival of breast tumor cells (Scheme 1). Overall, the novel bio-nanoplatform GDNPs@ICG substantially enhanced the photo-mediated anti-breast tumor therapy effect and could be an alternative for precise and efficient anti-tumor phototherapy.

Materials and Methods

Materials

The ginger used in this study is fresh Yunnan small yellow ginger, which belongs to the genus Zingiber officinale of the family Zingiberaceae. ICG, adriamycin (DOX), and 6-shogaol were purchased from Yuanye Bio-Technology Co., Ltd. (Shanghai, China). DMEM medium was purchased from Gibco (Waltham, MA, USA). Fetal bovine serum (FBS) was purchased from NEWZERUM (New Zealand). Cell Counting Kit-8 (CCK-8) was purchased from Apex Bio (Houston, USA). 4-Phenylbutanoic acid was purchased from MedChemExpress (New Jersey). Vitamin E (VE), Reactive Oxygen Detection Kit, 4′, 6-diamidino-2-phenylindole (DAPI), DIO (cell membrane green fluorescent probe), ER-Tracker Red (endoplasmic reticulum red fluorescent probe), senescence β-galactosidase Staining Kit (C0602), CY3-labelled goat anti-rabbit IgG (H + L), and Alexa Fluor 488 labelled goat anti-rabbit IgG (H + L) were purchased from Beyotime Institute of Biotechnology (Shanghai, China). β-tubulin rabbit pAb and Phospho-eIF2α-S51 Rabbit mAb were purchased from ABclonal Technology (Wuhan, China). Anti-eIF2α, Anti-GRP78/BiP, anti-PERK, anti-P-PERK (T982), and anti-CHOP Rabbit pAbs were purchased from Wanleibio (Shenyang, China). The MitoTracker Red CMXRos mitochondrial red fluorescent probe, Lyso-Tracker Red (lysosomal red fluorescent probe), and N-acetyl-l-cysteine were purchased from Solarbio (Beijing, China). The malondialdehyde (MDA) assay kit (TBA method) was purchased from the Nanjing

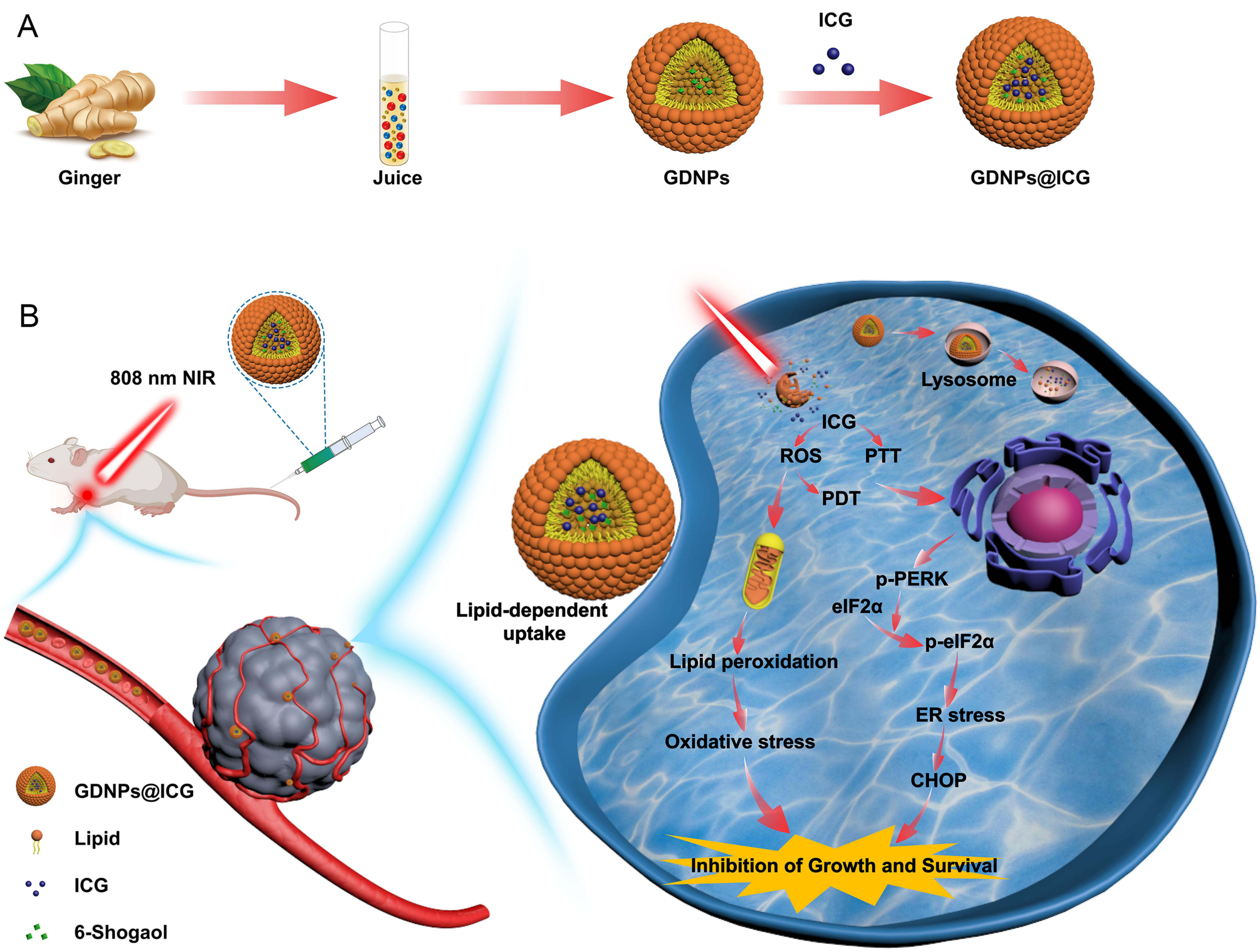

Scheme 1 Schematic illustration of the preparation and the anti-breast tumor mechanism of GDNPs@ICG. (**A**) The main preparation steps of GDNPs@ICG. (**B**) After intravenous administration, GDNPs@ICG are delivered to the tumor microenvironment through the EPR effect and uptake by tumor cells in a lipid-dependent manner. ICG, 6-shogaol and lipid fragments are released after lysosomal degradation or cleavage by 808 nm NIR laser. ICG, as a photosensitizer, produces a large amount of ROS and local hyperthermia, which causes lipid peroxidation and ER stress, thus inhibiting growth and survival of breast tumor cells.

Jiancheng Bioengineering Institute (Nanjing, China). Mouse ELISA kit for IL-6 (E-EL-M0044C) were purchased from Elabsience.

Isolation and Purification of GDNPs

GDNPs were extracted from fresh small yellow ginger by ultracentrifugation. Briefly, fresh ginger was peeled, chopped, and soaked in pre-cooled phosphate-buffered saline (PBS) solution. The juice was extracted and centrifuged at 1000 g for 30 min at 4°C. The supernatant was collected by centrifugation at 3000 g for 40 min to eliminate fibers and ginger tissues. The supernatant was centrifuged at 10,000 g for 1 h to remove cells and cellular debris, and further centrifuged at 50,000 g for 1 h to remove larger particles. The resulting precipitate was collected by centrifugation at 130,000 g for 1.5 h. The precipitate was then resuspended in cold PBS. The final centrifugation step was repeated twice to obtain GDNPs.

Preparation of GDNPs@ICG

ICG and GDNPs were added to flasks at a 1.5:1 ratio. The mixture was stirred at 37°C for 3 h in the dark. The resulting GDNPs@ICG were suspended in pre-cooled PBS via centrifugation at 130,000 g for 1.5 h at 4°C. Finally, GDNPs@ICG was stored at −80°C for further use. The ICG content in the supernatant after centrifugation was determined using a Uv-vis spectrophotometer (780 nm). Drug loading content (DLC) and drug encapsulation efficiency (DEE) were calculated using the following equations: DLC (%) = ($\text{Mass}_{\text{total ICG}}$ – $\text{Mass}_{\text{unloaded ICG}}$)/ ($\text{Mass}_{\text{GDNPs}}$ + $\text{Mass}_{\text{loaded ICG}}$) × 100; DEE (%) = ($\text{Mass}_{\text{total ICG}}$ – $\text{Mass}_{\text{unloaded ICG}}$)/$\text{Mass}_{\text{total ICG}}$ × 100.

Characterizations of GDNPs and GDNPs@ICG

The nanoparticle size and zeta potential of hydrated GDNPs@ICG were measured using a Malvern Zetasizer Nano ZS instrument (Malvern Instruments, UK). Meanwhile, the GDNPs@ICG were resuspended in PBS and stored at 4°C for one week, with the particle size of the nanoparticles measured on a daily basis. The morphology of GDNPs and GDNPs@ICG was observed using transmission electron microscopy (TEM) (FEI Tecnai G2F30 STWIN, USA) and scanning electron microscopy (SEM) (FEI Nova Nano SEM 450, USA). Fourier transform infrared spectrometry (FT-IR) (IRAffinity-1S, JPN) and Uv-vis spectrophotometry (Thermo ScientificTM Evolution 300, USA) were used to assess the drug-carrying properties of GDNPs. The 6-shogaol standard curve was plotted using HPLC (Waters Alliance HPLC, USA) according to the method described in the literature, and the content of 6-shogaol in GDNPs was determined.[37,38]

In Vitro Drug Release

To evaluate the release of ICG from the GDNPs@ICG nanoparticles in vitro, the quantity of ICG released was measured with or without NIR laser irradiation. The pH 7.4 solution is designed to simulate the pH of plasma, while the pH 6.5 solution is intended to simulate the pH of the tumor microenvironment. The pH 5.3 solution is formulated to simulate the pH of intracellular lysosomes. Suspensions of GDNPs@ICG (130 μg/mL ICG) at pH 7.4, were placed in dialysis bags (MW = 8000). The dialysis bags were immersed in PBS at different pH values (5.3, 6.5, and 7.4) and shaken horizontally (100 rpm) in a shaker at 37°C, and the absorbance of the solution was recorded at different time intervals (0, 2, 4, 6, 8, 10, 12, 24, 36, 48, 60, and 72 h) using a microplate reader. The amount of ICG released was calculated using the ICG standard curve. Cumulative drug release was calculated as follows: cumulative release (%) = M_t/M_a × 100%. M_t represents the content of the released ICG and M_a represents the gross ICG content in GDNPs@ICG.

Photothermal Properties of GDNPs@ICG

To assess the photothermal performance of GDNPs@ICG in vitro, different concentrations (1, 2.5, 5, 10, and 15 μg/mL ICG; 1 mL) of GDNPs@ICG were irradiated using an NIR laser (808 nm, 2.0 W/cm^2) for 10 min. A digital thermocouple was used to record the temperature at 1 min intervals. Infrared thermography was performed at 2 min intervals to observe the temperature increase in the GDNPs@ICG suspensions. To calculate the photothermal conversion efficiency (η) of GDNPs@ICG, the GDNPs@ICG suspension (15 μg/mL ICG, 1.0 mL) and deionized water were subjected to NIR laser irradiation (2.0 W/cm^2) for 10 min. Subsequently, the temperature was recorded at 1 min intervals.

Hemolysis Assay

The hemocompatibility of GDNPs@ICG was evaluated using a hemolysis test. Briefly, fresh whole blood was collected from the orbital venous plexus of mice, and the supernatant was removed. The precipitated red blood cells were washed three times with PBS. Subsequently, 50 μL of the red blood cell suspension was added to different concentrations of the GDNPs@ICG suspension (1.0 mL). Deionized water and PBS were used as positive and negative controls, respectively. The mixtures were shaken at 100 rpm for 4 h at 37°C and then centrifuged at low speed. The absorbance of the supernatant was measured at 540 nm using a microplate reader to calculate the hemolysis rate using the following formula:

Hemolysis (%) = (A_{Sample} - A_{Negative})/ (A_{Positive} - A_{Negative}) × 100

A_{Positive} and A_{Negative} refer to the absorbance of deionized water and PBS, respectively. A_{Sample} is the absorbance of the sample.

Cell Culture

The mouse 4T1 breast tumor cell line was purchased from the Institute of Basic Medical Sciences, Chinese Academy of Medical Sciences (Beijing, China), and cultured in complete DMEM medium (Gibco, Massachusetts, USA) containing 10% FBS at 37°C and 5% CO_2.

Distribution of GDNPs in 4T1 Cells

4T1 cells were incubated with Dio-dye-labelled GDNPs for 6 h, followed by organelle staining. Mitochondria were stained with a mitochondrial red fluorescent probe (MitoTracker Red CMXRos, 1:10,000) for 45 min; ER was stained with an ER red fluorescent probe (ER-Tracker Red, 1:3000) for 30 min, and lysosomes were stained with a lysosomal red fluorescent probe (Lyso-Tracker Red, 1:15,000) for 2 h. Finally, confocal laser scanning microscopy (Leica DMI6000CS, GER) was used to observe the localization of GDNPs in different organelles.

Cellular Uptake Assay

Auto-fluorescent DOX was loaded into GDNPs to detect the nanoparticles. 4T1 cells were incubated with GDNPs@DOX (5 µg/mL DOX) for 1, 2, or 4 h. Flow cytometry and confocal laser scanning microscopy were used to analyze the cellular uptake rate.

In Vitro Cytotoxicity Assay

The cytotoxicity of the nanoparticles on 4T1 cells was assessed using the CCK-8 assay. The 4T1 cells were seeded in 96-well plates at a density of 1.0×10^4 cells/well. In the no-laser irradiation group, the cells were incubated with different concentrations of ICG, GDNPs, or GDNPs@ICG (1, 2.5, 5, 10, and 15 µg/mL ICG and 5, 12.5, 25, 50, and 75 µg/mL GDNPs) for 24 h. Then, CCK-8 solution (10 µL) was added to each well. The cells were incubated for 2 h and the absorbance was determined using a microplate reader at 450 nm. In the NIR laser irradiation group, cells were incubated with different concentrations of ICG or GDNPs@ICG for 6 h and then irradiated with an NIR laser (808 nm, 2.0 W/cm^2) for 5 min. After a total incubation period of 24 h, the CCK-8 assay was performed, as described above.

ROS Production

The capacity of GDNPs@ICG to generate ROS was assessed using a 2.7-dichlorofluorescein diacetate (DCFH-DA) Reactive Oxygen Detection Kit. Briefly, for qualitative evaluation, 4T1 cells were incubated with ICG or GDNPs@ICG (5 µg/mL ICG and 25 µg/mL GDNPs) for 6 h. After dark or laser treatment, 4T1 cells were labelled with 10 µM DCFH-DA for 20 min at 37°C, followed by observation using an inverted fluorescence microscope. For quantitative assessment, fluorescence intensity was determined using a microplate reader with an excitation wavelength of 488 nm and an emission wavelength of 525 nm.

Lipid Peroxidation Assay

The cells in the culture dish were cultured to approximately 70% confluence. Subsequently, different concentrations of GDNPs@ICG (1, 2.5, 5, 10, and 15 µg/mL ICG, and 5, 12.5, 25, 50, and 75 µg/mL GDNPs) were added. After 6 h of incubation, the medium was refreshed and NIR laser irradiation was performed for 5 min. MDA content in the different groups of cells was determined to determine the level of lipid peroxidation. 4T1 cells were preincubated with the ROS scavenger N-acetylcysteine (NAC), a lipid peroxidation inhibitor (Vitamin E, VE), or an ER stress inhibitor, 4-phenyl-butyric acid (4-PBA), for 24 h in a 6-well plate. Subsequently, GDNPs@ICG suspensions (10 µg/mL ICG) were added and incubated for 6 h. The cells were treated with an 808 nm laser for 5 min and then stabilized for 3 h. The absorbance of MDA was measured at 532 nm.

Western Blot (WB) Analysis

The cells were treated with different formulations for 24 h and lysed for WB analysis. A BCA Protein Analysis Kit was used to quantify the protein concentration. The samples were then boiled for 10 min. The protein samples obtained were separated with 10% sodium dodecyl sulfate-polyacrylamide gel electrophoresis (SDS-PAGE) and then transferred to polyvinylidene fluoride (PVDF) membrane (Millipore). After sealing the PVDF membrane with 5% non-fat milk for 1 h, the membrane was incubated with a primary antibody overnight at 4°C, followed by incubation with an HRP-conjugated secondary antibody for 1 h at room temperature and chemiluminescence imaging (BG-gdsAUTO710 MINI, China) was performed.

In Vivo Animal Model

Six-week-old female BALB/c mice were obtained from Liaoning Changsheng Biotechnology Co., Ltd., and used to establish tumor-bearing animal models of 4T1 breast tumor. All animal experiments were conducted in accordance with the National Institute Guide for the Care and Use of Laboratory Animals and approved by the Institutional Animal Care and Use Committee of Shengjing Hospital of China Medical University (approval number: 2024PS156K). 4T1 cells (1.0×10^6 cells/mouse) were injected subcutaneously into the right armpit of the mice. When the tumor volume reached 50–100 mm^3, the mice were randomly divided into five groups (n=4): (a) PBS, (b) GDNPs, (c) ICG + Laser, (d) GDNPs@ICG, and (e) GDNPs@ICG + Laser. Mice in each group were intravenously injected with different formulations (3.75 mg/kg equivalents ICG per mouse). After 24 h post-administration, the tumor areas in the (c) and (e) groups of mice were irradiated with an 808 nm laser (2.0 W/cm^2) for 5 min. During NIR laser irradiation, the tumor area was monitored using infrared thermography. On day 1, 4, and 7, three treatments were administered and the size of the tumors and body weight of the mice were measured every two days. The tumor volume was calculated using the following formula: $[\text{length} \times (\text{width})^2] /2$. Blood samples were collected for biochemical analysis of serum. Tumor tissues and major organs (the heart, liver, spleen, lung, and kidney) were collected for histological analysis. Sections of the major organs of the mice were prepared and stained with hematoxylin-eosin (H&E).

Immunofluorescence Staining

The tumor tissue sections were heated at 65°C for 2 h, immersed in xylene for 15 min, and sequentially immersed in 100%, 95%, and 75% ethanol. After three rinses, the sections were antigenically repaired with citric acid and blocked with 10% goat serum for 30 min at 37°C. Subsequently, the sections were incubated overnight with the primary antibody, followed by 1h incubation with the secondary antibody at 37°C. The antibodies used were N-cadherin polyclonal antibody (1:500, Proteintech, 22018-1-AP), CD31 polyclonal antibody (1:1000, Proteintech, 28083-1-AP), IFN gamma rabbit pAb (1:500, Bioss, bs-0480R), and CD8 Rabbit pAb (1:500, Bioss, bs-0648R).

Detection of IL-6 Expression in Mouse Tumor Tissues by ELISA

Tumor tissues were extracted from each group of mice and homogenized using a glass homogenizer. The samples were then centrifuged and the resulting supernatant was analyzed for IL-6 expression using a commercial ELISA kit.

Senescence-Associated β-Galactosidase Assay

The 4T1 cells were treated with GDNPs, ICG, and GDNPs@ICG for 6 h. The cells in the ICG and GDNPs@ICG-treated groups were irradiated with an 808 nm, 1.0 W/cm^2 NIR laser for 3 min, and then returned to the incubator for continuous culture, and changes in cell morphology were observed. Staining was performed using an SA-β-gal staining kit (Beyotime, China; C0602). Finally, the SA-β-gal-positive cells were observed under an ordinary optical microscope.

Detection of Senescence Associated Markers Expression by RT-qPCR

RT-qPCR was used to detect the expression of senescence-associated markers, including p16, p21, and p53 in the tumor tissues. Total RNA was extracted using TRIzol reagent according to the manufacturer's instructions (Invitrogen). RNA was reverse transcribed to cDNA using PrimeScript™ RT Master Mix, and RT-qPCR was performed on a Roche LightCycler® 96 real-time qPCR system in a 20 μL reaction volume using a TB Green® Premix Ex Taq™ II (Tli RNaseH Plus) kit. All primers were purchased from Sangon Bioengineering Co. Ltd. (Shanghai, China). The primer sequences used for RT-qPCR are listed in Table 1.

Statistical Analysis

All results were expressed as mean ± SD, and statistical analyses were performed using Origin 2021 or GraphPad Prism 8 software, with one-way ANOVA and Tukey's Honest Significant Difference (HSD) test for multiple comparisons. *$P<0.05$, ** $P<0.01$, *** $P<0.001$.

Table 1 The Sequences of the Primers

Gene name	Sequences	
p16	Forward	5'- CTTTCGGTCGTACCCCGATT-3'
	Reverse	5'- TACGTGAACGTTGCCCATCA-3'
p21	Forward	5'- TTGTCGCTGTCTTGCACTCT-3'
	Reverse	5'- TTTCGGCCCTGAGATGTTCC-3'
p53	Forward	5'- CCATGGCCCCCCTGTCATCTTT-3'
	Reverse	5'- GAAGCCATAGTTGCCCTGGT-3'
GAPDH	Forward	5'- GAGAGTGTTTCCTCGTCCCG-3'
	Reverse	5'- ATCCGTTCACACCGACCTTC-3'

Results

Preparation and Characterization of GDNPs@ICG

We first determined the nanoparticle size and zeta potential of the GDNPs and GDNPs@ICG. As shown in Figure 1A, dynamic light scattering (DLS) revealed that GDNPs had an average hydrodynamic diameter of approximately 108.6 ±2.60 nm and a relatively low polydispersity coefficient (PDI, 0.217). GDNPs@ICG were prepared by loading ICG into GDNPs by co-incubation. The average hydrodynamic diameter of GDNPs@ICG measured by DLS increased to approximately 134.3±3.04 nm, and the PDI was 0.221 (Figure 1B). The GDNPs@ICG nanoparticles were stored at 4 °C for one week in a PBS solution. No significant change in particle size was observed during this period, indicating that the nanoparticles exhibited good stability (Supplementary Figure 1). The zeta potentials of GDNPs and GDNPs@ICG were −7.16±1.35 mV and −10.72±0.75 mV respectively (Figure 1C). SEM and TEM were used to observe the morphology of GDNPs and GDNPs@ICG. Both nanoparticles are rough spheres with particle sizes of 100.0 nm and 124.0 nm, respectively (Figure 1D–G). The protein content of ginger juice and GDNPs was compared using SDS-PAGE, as shown in Figure 1H. These results indicated that the proteins in the ginger cells were retained in the GDNPs. Furthermore, thin-layer chromatography revealed that the GDNPs contained various types of lipids (Figure 1I). The content of 6-shogaol in GDNPs was 0.63 μg per mg of protein determined by HPLC. Furthermore, GDNPs@ICG exhibited the characteristic ultraviolet absorption peak of ICG at 780 nm (Figure 1J). The functional groups of GDNPs@ICG were characterized using FT-IR spectroscopy. The overall FT-IR peak pattern of GDNPs@ICG closely resembled that of the ICG. The characteristic absorption peak of the sulfonic acid group was observed at 1091 cm^{-1}, while the absorption peak of C = C was observed at 1649 cm^{-1} (Figure 1K). This result demonstrated that the co-incubation method did not alter the chemical structure of the drug molecules, and ICG was effectively loaded into the GDNPs. The ICG load efficiency was 19.86%. The drug release curve of GDNPs@ICG showed that 69.35% of the ICG was released at pH 5.3. At pH 7.4, only 18.06% of ICG was released from GDNPs@ICG. These findings indicated that in a neutral environment, GDNPs were more stable and can effectively prevent the release of ICG. However, in a slightly acidic environment, GDNPs underwent rupture, which promoted the release of ICG from GDNPs@ICG nanoparticles. Under NIR laser irradiation at pH 7.4, GDNPs@ICG released 22.75% of ICG, significantly more than the non-laser-irradiated group, indicating that GDNPs@ICG had photothermal drug release behavior (Figure 1L). These results demonstrated that an acidic environment and laser irradiation promoted the rupture and degradation of GDNPs, facilitating the release of ICG.

Photothermal Properties of GDNPs@ICG

To evaluate the photothermal performance of GDNPs@ICG, we investigated the photothermal heating capacity of different concentrations of GDNPs@ICG under 808 nm NIR laser irradiation. GDNPs@ICG suspensions (1, 2.5, 5, 10, and 15 μg/mL ICG) were exposed to an 808 nm NIR laser (2.0 $\mathrm{W/cm}^2$) for 10 min, and PBS was used as the control group. With an increase in temperature, the GDNPs@ICG suspensions exhibited concentration and irradiation time dependence (Figure 2A and B). Under continuous laser irradiation, the maximum temperature of GDNPs@ICG at a concentration of 15 μg/mL could reach 53.1°C. To observe the heating of GDNPs@ICG more

https://doi.org/10.2147/IJN.S478435

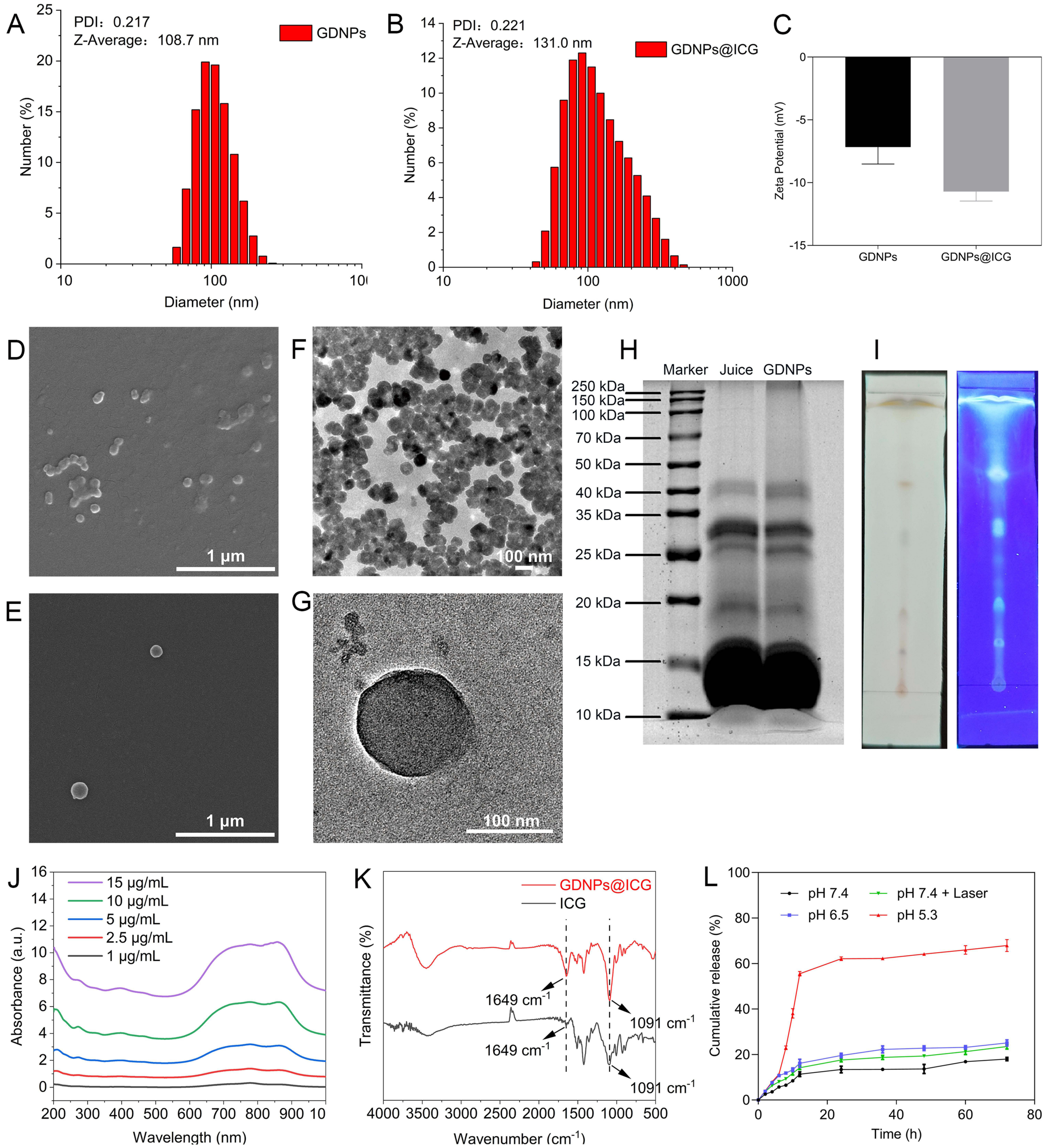

Figure 1 Preparation and characterization of GDNPs@ICG. (**A-B**) The average hydrodynamic sizes of GDNPs and GDNPs@ICG measured by DLS. (**C**) Zeta-potential of GDNPs and GDNPs@ICG. Data are expressed as mean ± SD (n = 3 independent samples). (**D-E**) SEM images (scale bar = 1 μm) of GDNPs and GDNPs@ICG. (**F-G**) TEM images (scale bar = 100 nm) of GDNPs and GDNPs@ICG. (**H**) SDS-PAGE protein analysis of ginger and GDNPs. (**I**) Total lipids were extracted from GDNPs using chloroform and analyzed through thin-layer chromatography. (**J**) The Uv-vis spectra of different concentrations of GDNPs@ICG. (**K**) The FT-IR spectra of ICG and GDNPs@ICG. (**L**) The in vitro release profiles of ICG from GDNPs@ICG in PBS solutions (pH 5.3, pH 6.5 or pH 7.4) at 37°C in the presence or absence of NIR light irradiation.

intuitively, an infrared thermography camera was used to photograph the suspensions of GDNPs@ICG at different concentrations every 2 min during NIR laser irradiation, and the heating of the solutions was recorded (Figure 2C). Before the start of the experiment, the IR thermography of the different groups of solutions showed a temperature of approximately 24–26°C, which was similar to that of the laboratory. The temperature of the GDNPs@ICG gradually

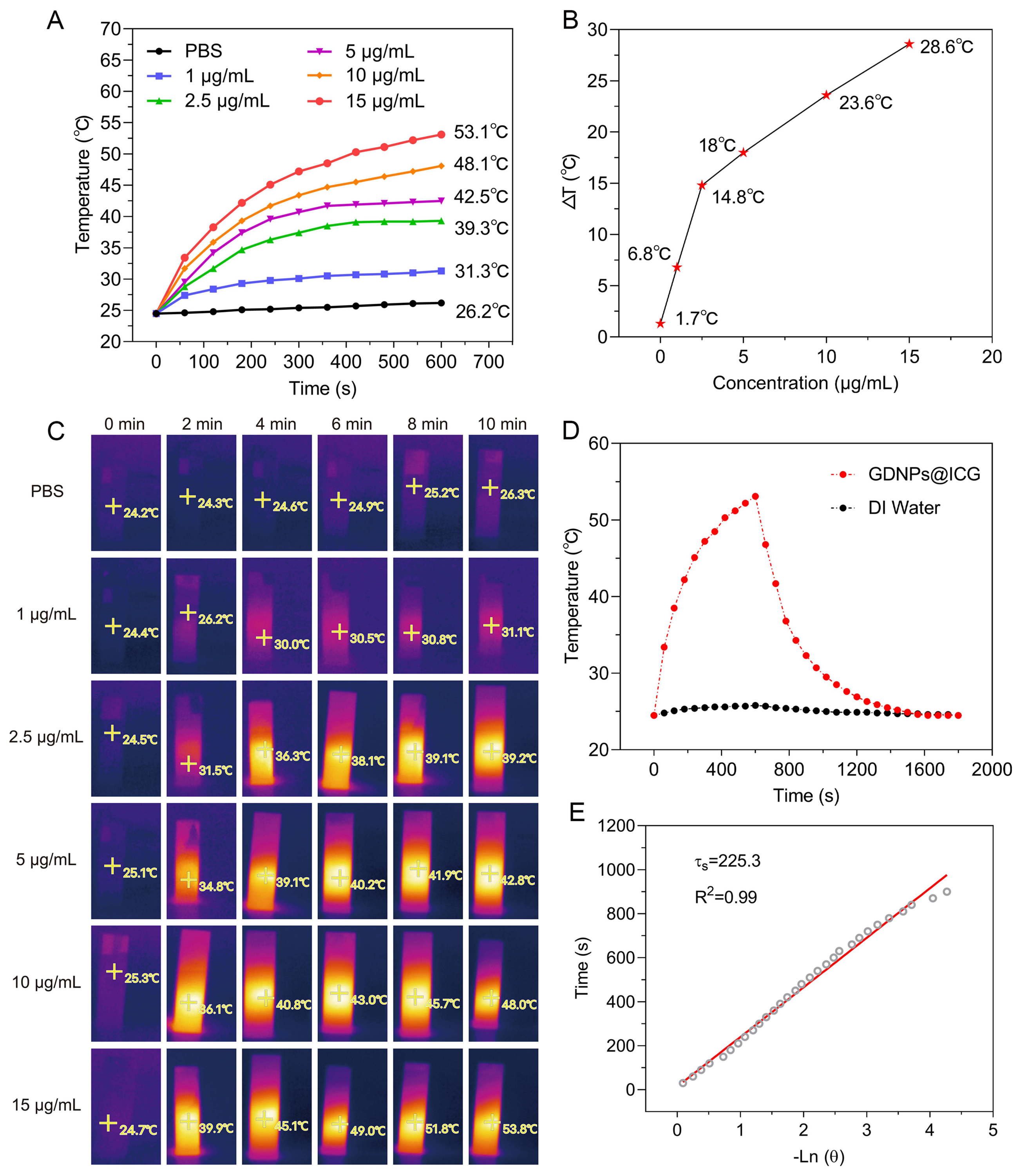

Figure 2 Photothermal performance study of GDNPs@ICG. (**A**) Temperature versus time and (**B**) temperature change of GDNPs@ICG at different concentrations after NIR laser irradiation (808 nm, 2.0 W/cm^2) for 10 min. (**C**) Infrared thermal images of GDNPs@ICG suspension under NIR laser irradiation. (**D**) Heating and cooling curves of GDNPs@ICG suspension (15 μg/mL ICG) and deionized water. (**E**) Relationship between cooling time and negative natural logarithm of the temperature gradient. The time constant of heat transfer was measured to be τ_S = 225.3 s.

https://doi.org/10.2147/IJN.S478435

increased in an irradiation time- and concentration-dependent manner. When the concentration of the GDNPs@ICG suspension was 15 μg/mL, the temperature increased to 53.8°C after 10 min of 808 nm laser irradiation. The temperature of the PBS group rose from 24.2°C initially to 26.3°C with little change in temperature. Similarly, the heating and cooling of GDNPs@ICG (15 μg/mL ICG) and deionized water were measured using digital thermocouples, which were consistent with the infrared thermography results (Figure 2D). These results indicated that GDNPs@ICG exhibited a strong photothermal conversion performance. Besides, the value of the time constant τ_s was determined to be 225.3 s from the cooling cycle curve (Figure 2E), and the photothermal conversion efficiency η of GDNPs@ICG was about 26.38%, which was higher than most of the previously reported nanomaterials, such as gold nanoshells (13%), gold nanocrystals (21.0%), gold nanorods (22%), and prussian blue nanoparticles (22.91%).[39,40] These results confirmed the excellent potential of GDNPs@ICG to induce photothermal ablation of tumor cells.

In Vitro Cellular Uptake and Distribution of GDNPs@ICG in Tumor Cells

Before investigating the therapeutic effect of GDNPs@ICG, we evaluated its cellular uptake and distribution in the 4T1 breast tumor cells. For the in vitro cellular uptake study, auto-fluorescent DOX was loaded into the GDNPs as a fluorescent dye instead of ICG. Flow cytometry and confocal microscopy showed that the cellular uptake of GDNPs@DOX increased with increasing incubation time (Figure 3A and B), suggesting that GDNPs@DOX was effectively internalized by 4T1 cells. To investigate the distribution of GDNPs in tumor cells, Dio-labelled GDNPs were co-incubated with 4T1 cells, and different cellular compartments, including the ER, lysosomes, and mitochondria, were stained with the corresponding fluorescent probes. Confocal microscopy revealed extensive accumulation of GDNPs in the ER, lysosomes, and mitochondria of the 4T1 breast tumor cells (Figure 3C).

In Vitro Therapeutic Effects of GDNPs@ICG

Next, we evaluated the in vitro therapeutic effects of GDNPs@ICG on the 4T1 breast tumor cells. It was found that cell viability was not inhibited at different concentrations in either the ICG or GNDPs group, which indicated that ICG or GNDPs had limited toxicity to tumor cells. However, the ICG + Laser, GDNPs@ICG, and GDNPs@ICG + Laser groups exhibited significant concentration-dependent reductions in tumor cell viability. The GDNPs@ICG + Laser group showed the highest tumor-killing ability (Figure 4A). Next, 4T1 cells were incubated with GDNPs@ICG in the presence of the ROS scavenger N-acetylcysteine (NAC), the lipid peroxidation inhibitor VE, or the ER stress inhibitor 4-phenylbutyric acid (4-PBA) and irradiated with an 808 nm laser (2.0 W/cm^2, 5 min). The viability of 4T1 cells was significantly restored in the presence of NAC, VE, or 4-PBA compared to the control group, suggesting that the ability of GDNPs@ICG to inhibit cell viability was associated with ROS production, lipid peroxidation, and ER stress (Figure 4B). Furthermore, we evaluated the ability of GDNPs@ICG to generate ROS by using a DCFH-DA probe. Compared with those without laser irradiation, both the ICG + Laser and GDNPs@ICG + Laser groups produced higher levels of ROS (Figure 4C and D). To further investigate the role of lipid peroxidation in this process, we measured the levels of MDA, a classical marker of lipid peroxidation. After 4T1 cells were co-incubated with GDNPs@ICG and subsequently subjected to laser irradiation, the level of MDA in the tumor cells significantly increased with increasing concentrations of GDNPs@ICG (Figure 4E). In addition, in the presence of NAC or VE, the cells produced lower levels of MDA (Figure 4F), suggesting that ROS generation may contribute to lipid peroxidation and inhibit the growth and survival of tumor cells. The expression of proteins associated with ER stress was also detected by WB analysis (Figure 4G). It was found that, compared with the control PBS group, the GDNPs group or ICG group itself had relatively less effect on the expression of ER stress-related proteins. However, the GDNPs@ICG, ICG + Laser, and GDNPs@ICG + Laser groups showed significantly upregulated expression of BiP, p-PERK, p-eIF2α, and CHOP. The upregulation was more pronounced in the GDNPs@ICG + Laser group. Therefore, in the GDNPs@ICG with laser irradiation group, the synergistic interaction between ICG and GNDPs triggered ROS generation, induced lipid peroxidation, and enhanced ER stress, which eventually inhibited the growth and survival of breast tumor cells.

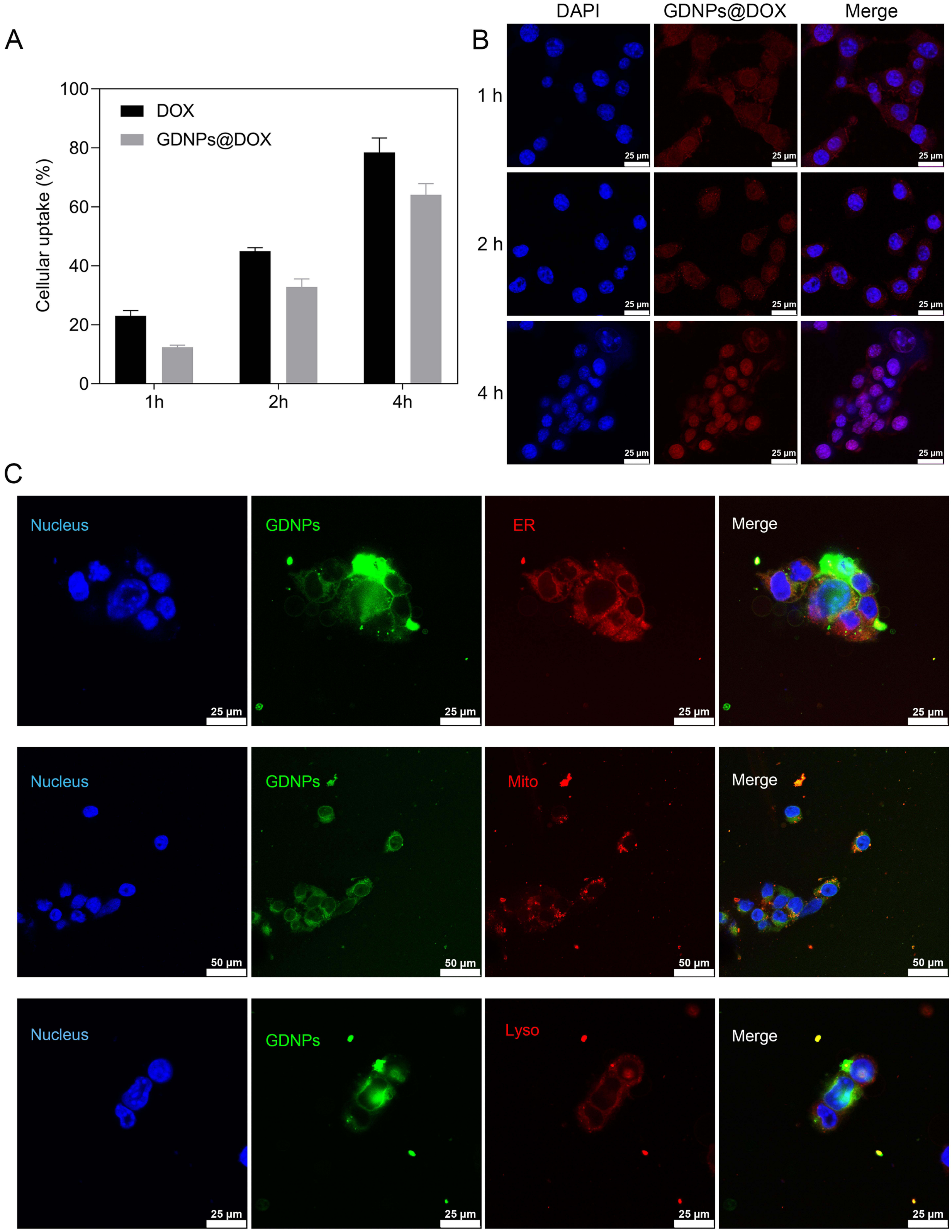

Figure 3 In vitro cellular uptake and distribution of GDNPs@ICG in tumor cells. (**A**) Quantitative analysis of cellular uptake of GDNPs@DOX by flow cytometry. (**B**) Confocal images of 4T1 cells incubated with GDNPs@DOX for 1, 2 or 4 h. Scale bar is 25 μm. (**C**) Confocal images representing the distribution of Dio-labelled GDNPs in 4T1 cells. Lysosomes, mitochondria, and ER were stained with Lyso-Tracker Red, MitoTracker Red CMXRos, and ER-Tracker Red, respectively. The nuclei were stained blue by Hoechst 33258.

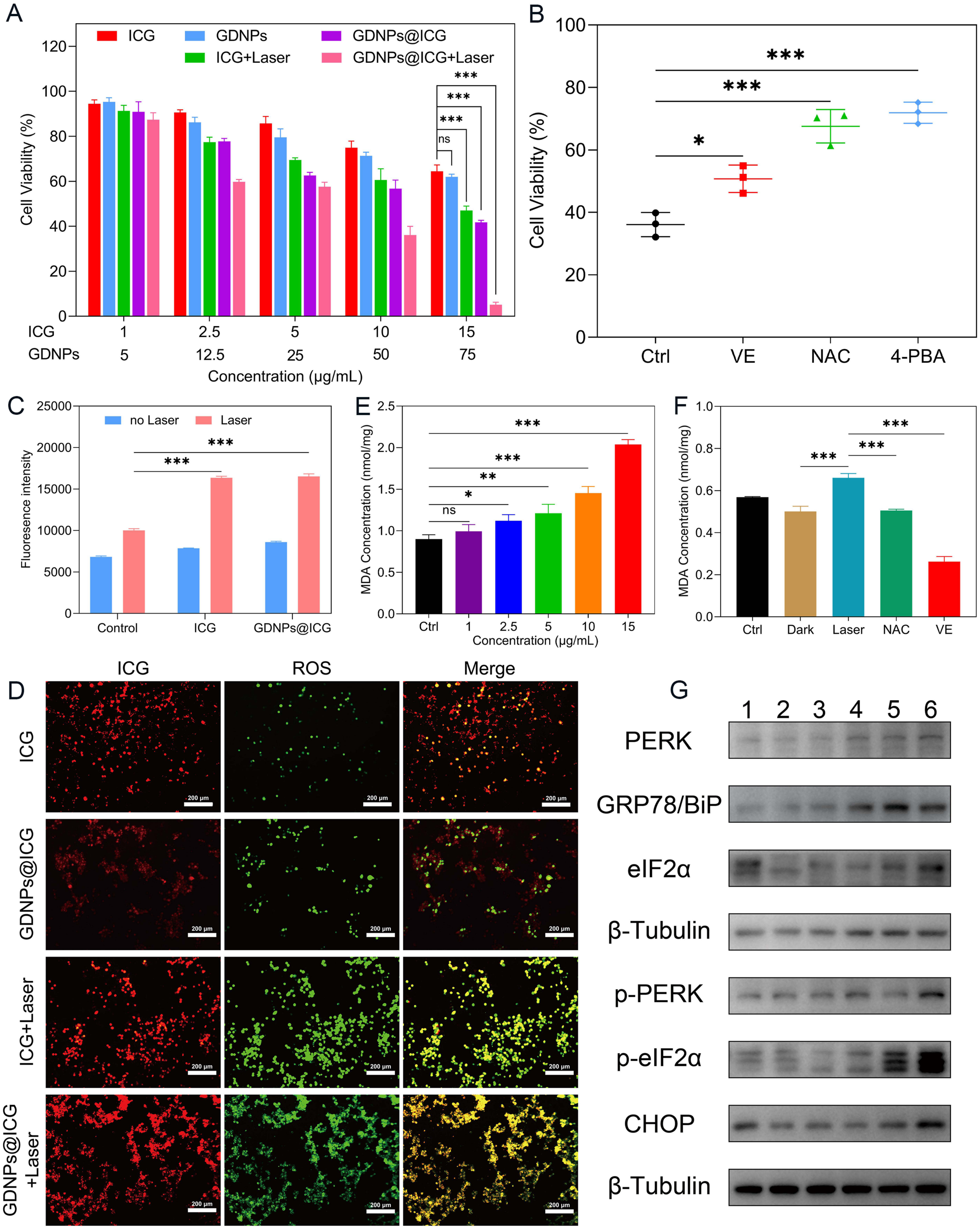

Figure 4 In vitro therapeutic effects of GDNPs@ICG. (**A**) Cytotoxicity of different concentrations of ICG, GDNPs and GDNPs@ICG in 4T1 cells irradiated with or without 808 nm laser (2.0 W/cm^2, 5 min). (**B**) Cytotoxicity of GDNPs@ICG (10 μg/mL ICG) on 4T1 cells in the presence of NAC, VE and 4-PBA. Ctrl was the control group without any addition of inhibitors. (**C**) Quantification of ROS production in 4T1 cells by enzyme-labeled instrument. (**D**) CLSM images of 4T1 cells co-incubated with ICG and GDNPs@ICG (5 μg/mL ICG) irradiated with or without an 808 nm laser (2.0 W/cm^2, 5 min). ROS was detected by DCFH-DA. The scale bar is 200 μm. (**E**) Changes in the levels of MDA in 4T1 cells due to different administered concentrations of GDNPs@ICG (0, 1, 2.5, 5, 10 and 15 μg/mL ICG) during irradiation with 808 nm of NIR laser (2.0 W/cm^2, 5 min). (**F**) The concentration of MDA in 4T1 cells under different treatment conditions. (**G**) WB analysis of ER stress-related proteins. 1: PBS group; 2: GDNPs group; 3: ICG group; 4: GDNPs@ICG group; 5: ICG + Laser group; 6: GDNPs@ICG + Laser group. Data are expressed as mean ± SD (n = 3). Statistical significance was calculated using one-way ANOVA, and multiple comparisons were performed using the Tukey post-hoc test. * $P < 0.05$, ** $P < 0.01$, *** $P < 0.001$.

In Vivo Therapeutic Effects of GDNPs@ICG

The in vivo anti-tumor therapeutic effect of GDNPs@ICG was investigated in a 4T1-tumor-bearing mouse model. Mice were randomly divided into five groups: PBS, GDNPs, ICG + Laser, GDNPs@ICG, and GDNPs@ICG + Laser. Following drug administration or laser irradiation, the tumor volume and body weight of mice in different groups were measured every two days, and three treatments were administered on day 1, 4, and 7 (day 2, 5, and 8) (Figure 5A). The results showed that tumor volume rapidly increased in all non-laser-irradiated groups within 15 days; however, the growth of tumors in the NIR laser-irradiated groups was significantly inhibited. In particular, the tumor volume in the GDNPs@ICG + Laser group was 0.35 times that in the PBS group, 0.41 times that in the GDNPs group, 0.43 times that in the GDNPs@ICG group without laser irradiation and 0.51 times that in the ICG group with laser irradiation (Figure 5B). No detectable changes in the body weight of mice were observed during the treatment period (Figure 5C). The mean tumor weight in each group was consistent with the tumor volume (Figure 5D). The above results indicated that the GDNPs@ICG + Laser group had good biocompatibility in vivo, and NIR laser irradiation enhanced their anti-tumor ability. To evaluate the PTT efficacy of the nanoparticles during NIR laser irradiation, an infrared thermography camera was used to capture real-time thermal images of mice at specific time intervals (Figure 5E). The temperature increase at the tumor site in the GDNPs@ICG + Laser group was greater than that in the ICG + Laser group. This demonstrated that GDNPs@ICG achieved more efficient accumulation at the tumor site and enhanced the PTT effects.

In Vivo Toxicology Analysis of GDNPs@ICG

To evaluate the in vivo toxicity of GDNPs@ICG-mediated treatment, we collected blood from mice for routine biochemical examination. Additionally, the major organs (heart, liver, spleen, lung, and kidney) were collected from the mice and stained with hematoxylin and eosin for histological analysis. No significant differences were observed in the major blood indices, including red blood cells (RBC), hemoglobin (HGB), and platelets (PLT) (Figure 6A-C). Meanwhile, the liver injury indices (aspartate aminotransferase [AST], alanine aminotransferase [ALT]) and kidney injury indices (creatinine [CREA], blood urea nitrogen [UREA]) of mice in all treatment groups were within normal levels and did not differ significantly between the different research groups, suggesting that the treatment had no detrimental impact on liver and kidney functions (Figure 6D-F). The hemolysis experiment results showed that the hemolysis rates of GDNPs and GDNPs@ICG were both less than 5% (Figure 6G). Furthermore, histological analysis results indicated that the morphology of the major organs, including the heart, liver, spleen, lung, and kidney, in all mouse groups was normal and without significant pathological abnormalities (Figure 6H). These results demonstrate that GDNPs@ICG is biocompatible and has limited toxic effects on major organs.

GDNPs@ICG Suppressed Breast Tumor Malignant Behaviors

Using the above tumor tissues, we further investigated the mechanism of the GDNPs@ICG-mediated anti-breast tumor therapeutic effect in vivo. Angiogenesis plays an important role in tumor growth and metastasis. Overexpression of CD31 in tumor tissue is a classical marker of angiogenesis.[41,42] N-cadherin is a key protein that promotes the invasion and metastasis of tumor cells.[43–45] Immunofluorescence staining of tumor tissues revealed that GDNPs@ICG + Laser treatment resulted in a significant reduction in the expression levels of CD31 and N-cadherin proteins compared with the other groups (Figure 7A). These results demonstrated that GDNPs@ICG + Laser treatment significantly decreased angiogenesis within tumor tissues, thereby preventing the invasion and metastasis of breast tumor cells. ICD, achieved by PTT or PDT, induces an anti-tumor immune response by promoting the release of inflammatory factors.[46–48] We evaluated the expression of IFN-γ, CD8, and IL-6 in tumor tissues from the different treatment groups. It was found that the GDNPs@ICG + Laser treatment resulted in a significantly increased expression of IFN-γ and CD8 compared with other groups (Figure 7B). Meanwhile, the level of IL-6 was also remarkably increased in the GDNPs@ICG + Laser group (Figure 7C), indicating that the treatment could effectively activate the anti-tumor immune response. This enhanced local immune activity contributed to tumor shrinkage and regression. In addition, GDNPs@ICG + Laser

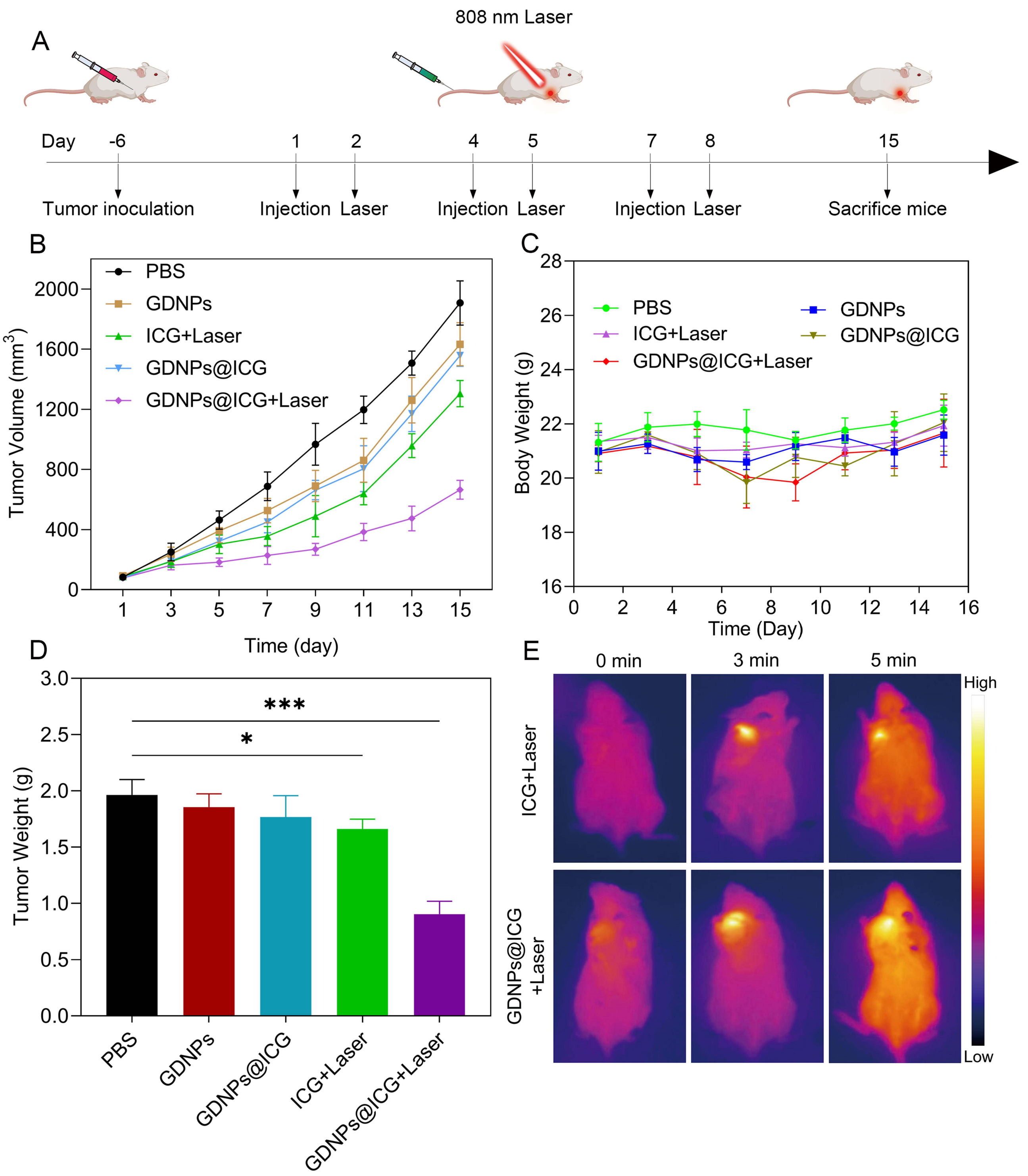

Figure 5 In vivo therapeutic effects of GDNPs@ICG. (**A**) Administration treatment protocol for 4T1-tumor-bearing mice. Mice were randomly divided into five groups: PBS, GDNPs, ICG + Laser, GDNPs@ICG, and GDNPs@ICG + Laser. (**B**) Changes in tumor volume in different groups of mice during treatment. (**C**) Changes in body weight of mice in different groups during treatment. (**D**) Mean weight of tumors collected from different groups of mice when mice were sacrificed after treatment on day 15. (**E**) In vivo INR thermal images of 4T1-tumor-bearing mice injected intravenously with ICG or GDNPs@ICG after irradiation by 808 nm laser (2.0 W/cm^2, 5 min). Data are expressed as mean ± SD (n = 4). Statistical significance was calculated using one-way ANOVA, and multiple comparisons were performed using the Tukey post-hoc test. * *P* < 0.05, *** *P* < 0.001.

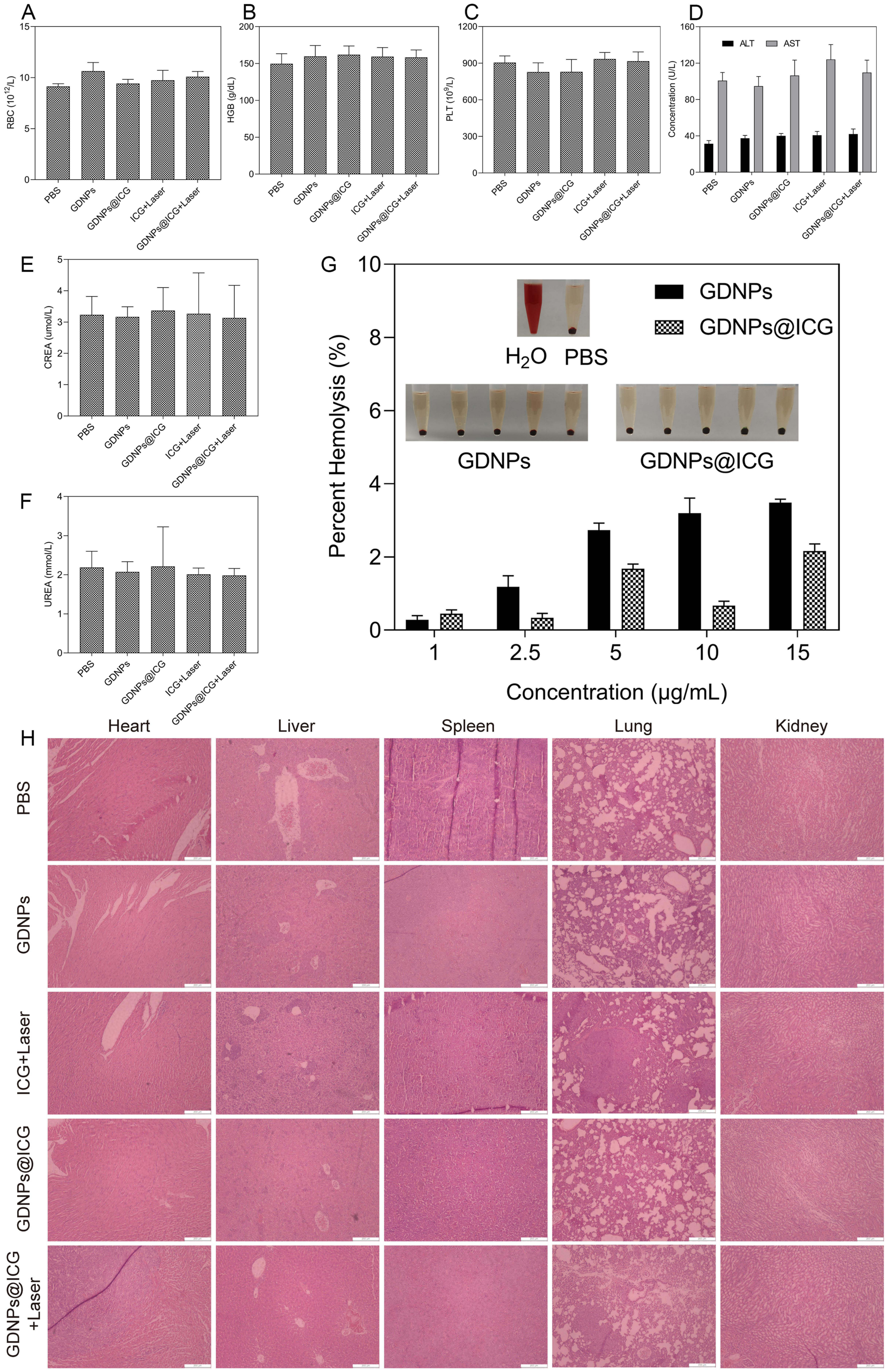

Figure 6 In vivo toxicology analysis of GDNPs@ICG. (**A-C**) Routine blood tests including RBC, HGB and PLT. (**D-F**) Blood biochemical tests for ALT and AST, CREA and blood UREA. (**G**) Hemolytic percent of red blood cells incubated with GDNPs or GDNPs@ICG at various concentrations for 4 h. Deionized water and PBS as the positive and negative controls, respectively. (**H**) H&E-stained images of major organs (including heart, liver, spleen, lung and kidney) of mice sacrificed on the 15th day. Scale bar is 200 µm.

https://doi.org/10.2147/IJN.S478435

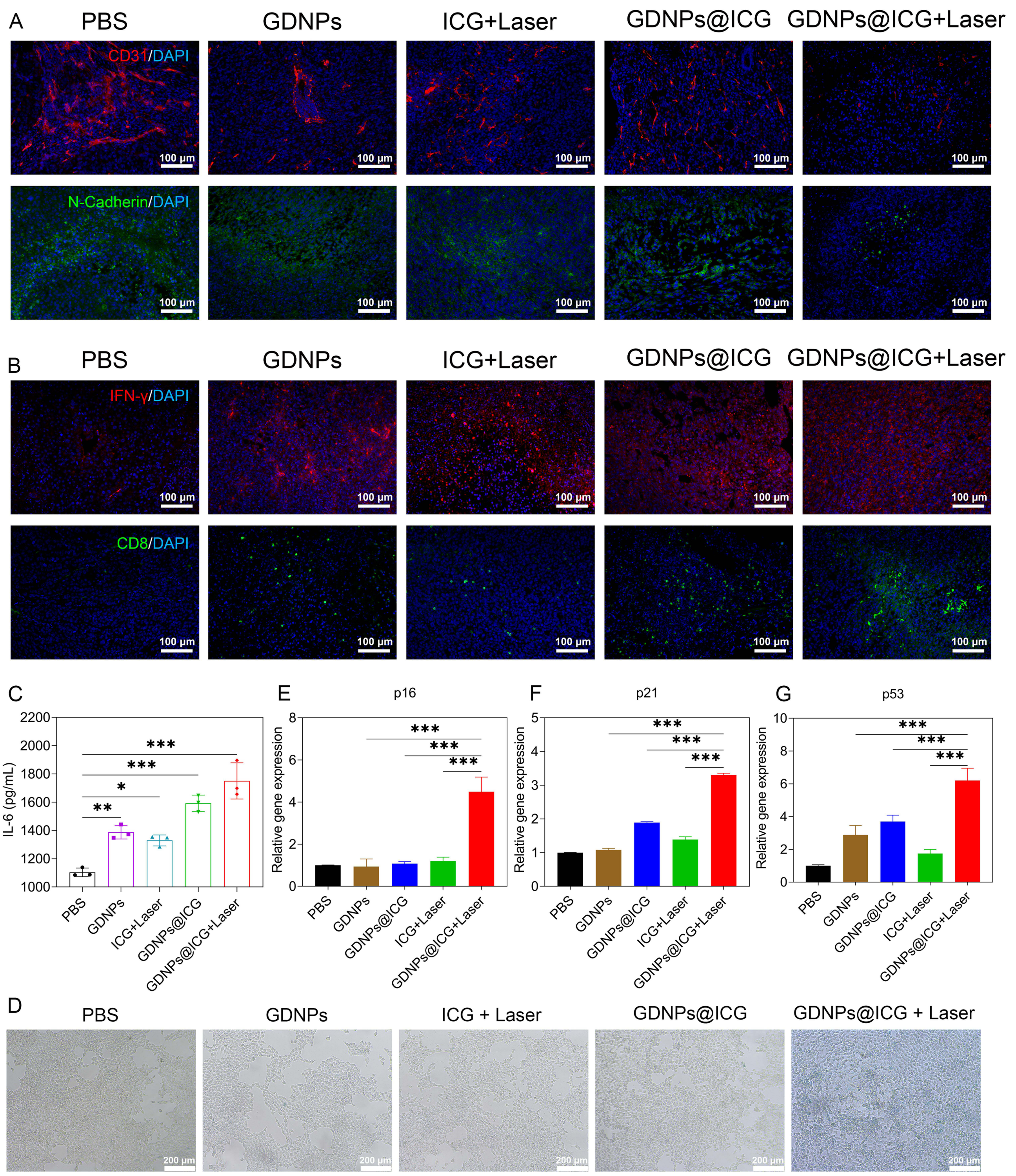

Figure 7 GDNPs@ICG suppressed breast tumor malignant behaviors. (**A**) Representative images of immunofluorescence staining of CD31 (red) and N-Cadherin (green) in mouse tumor tissue sections. The scale bar is 100 μm. (**B**) Representative images of immunofluorescence staining of IFN-γ (red) and CD8 (green) in mouse tumor tissue sections. The scale bar is 100 μm. (**C**) The expression level of IL-6 in mouse tumor tissues detected by ELISA. (**D**) Representative images of senescence-associated SA-β-gal staining (blue) in 4T1 cells after different treatments. The scale bar is 200 μm. (**E-G**) Expression of senescence-associated genes p16, p21, and p53 in mouse tumor tissues detected by RT-qPCR. n = 3, statistical significance was calculated using one-way ANOVA, and multiple comparisons were performed using the Tukey post-hoc test. * $P < 0.05$, ** $P < 0.01$, *** $P < 0.001$.

treatment significantly increased the senescence-related β-galactosidase activity in 4T1 breast tumor cells (Figure 7D). Meanwhile, the expression of genes that were closely related to senescence, including p16, p21, and p53, was also significantly upregulated in the tumor tissues of mice treated with GDNPs@ICG + Laser compared to other groups (Figure 7E-G). This further confirmed that the GDNPs@ICG + Laser promoted the senescence of breast tumor cells. These experimental results collectively demonstrated that the GDNPs@ICG nanoparticles not only inhibited tumor invasion and metastasis, but also activated immune responses and promoted tumor cell senescence.

Discussion

Owing to their easy obtainability, low cost, high yield, non-immunogenicity, limited toxicity and bio-compatibility,[49] GDNPs have been extensively applied in various areas, such as anti-inflammation,[25,50,51] anti-infection,[52] regulating of gut microbiota,[53] anti-virals,[54] and drug delivery.[55–58] However, the interactions between GDNPs and solid tumors are not well understood, especially the applications of GDNPs in enhancing anti-tumor therapy effects. Many researchers have identified that GDNPs are rich in lipids and the anti-tumor active ingredient, 6-shogaol,[25,59–62] implying that GNDPs might be easily taken up by tumor cells and possess potentially excellent anti-tumor ability. ICG, although the only FDA-approved NIR fluorescent dye for clinical use and widely utilized in phototherapy, including PTT and PDT,[63–66] still faces drawbacks such as poor stability in aqueous solutions, easy aggregation of molecules, and short plasma half-life.[13,67–70] To solve these issues, improve the bioavailability and tumor targeting of ICG, and utilize the potentially excellent anti-tumor ability of GDNPs, we built a novel bio-nanoplatform, GDNPs@ICG, based on GDNPs and ICG, which has been shown to substantially enhance the photo-mediated anti-breast tumor therapy effects.

In this study, both the newly developed GDNPs and GDNP@ICG were rough spheres with particle sizes of 100 and 124 nm, respectively. Investigations have confirmed that nanoparticles with a particle size of 50–200 nm can prolong the circulation time in the bloodstream and accumulate at the tumor site through the enhanced permeability and retention (EPR) effect.[71–73] Even in patient-derived xenograft models, nanoparticles can also present the clinical EPR effect.[74] Thus, our results indicate that GDNPs are good nano-delivery carriers. In addition, as for the photothermal properties of GDNPs@ICG, under laser irradiation, the maximum temperature of GDNPs@ICG could reach 53.1°C at the concentration of 15 μg/mL. High temperature (42–46°C) can cause irreversible cell damage, especially for tumor cells.[75,76] Therefore, owing to the obvious photothermal conversion advantage of GDNPs@ICG, ablation of tumor cells can be achieved with low doses of GDNPs@ICG. We further explored the in vitro cellular uptake and distribution of GDNPs@ICG in 4T1 breast tumor cells. According to previous studies, GDNPs have a membrane structure that is rich in lipids and serves as a raw material for the ER to synthesize lipids required for tumor lipid metabolism. Furthermore, GDNPs exhibit extensive interactions with mitochondria and lysosomes to maintain cellular homeostasis.[51,77,78] Besides GDNPs, other kinds of nanoparticles also interact with organelles to facilitate them uptake by the cell. Chen Q et al built a novel Metal-Phenolic Nanoparticles which could specifically target mitochondria.[79] Zeng J et al synthetized a novel biodegradable acid-activated acidifying nanoparticles as a lysosome targeting treatment which may restore lysosomal acidity and autophagy.[80] Purushothaman B et al even developed novel biotin-conjugated PEGylated porphyrin self-assembled nanoparticles to co-target mitochondria and lysosomes for advanced chemo-photodynamic combination therapy.[81] Our results are consistent with those of previous studies. GDNPs@ICG were taken up and effectively internalized by 4T1 cells and accumulated in the ER, mitochondria, and lysosomes.

Furthermore, we evaluated the therapeutic effects of GDNPs@ICG using in vitro and in vivo experiments. ICG, as a photosensitizer for PTT and PDT, can be excited by NIR light ranging from 750 nm to 810 nm, and we chose 808 nm NIR light for laser irradiation. Upon laser irradiation, even a relatively low concentration of GDNPs@ICG presented an excellent breast tumor-killing effect compared with free ICG, free GDNPs, ICG + Laser, or free GDNPs@ICG. The excellent anti-breast tumor ability of GDNPs@ICG may be attributed to the presence of anti-tumor 6-shogaol in GDNPs in addition to the effect of ICG. We hypothesized that, after internalization into breast tumor cells in a lipid-dependent manner, GDNPs@ICG would be broken down by lysosomes or fragmented via NIR light irradiation, releasing a significant quantity of lipids, ICG, and other components. Subsequently, a large amount of ROS was generated by ICG when exposed to laser radiation. Consequently, ROS may contribute to lipid peroxidation in 4T1 breast tumor cells.[82–84] Furthermore, excessive accumulation of intracellular lipids released from GDNPs@ICG causes lipotoxicity and disrupts intracellular lipid metabolic homeostasis. Both changes can act as endogenous stimuli to disrupt the normal function of the ER, resulting in the accumulation of large amounts of unfolded or misfolded proteins and induction of ER stress. Once this stress exceeds the unfolded protein response (UPR) effect and limits cell regulatory capacity, tumor cell growth and survival can be affected remarkably.[85–88] Based on the above hypothesis, we examined the levels of the relevant indicators. Upon laser irradiation, GDNPs@ICG significantly upregulated the levels of ROS, MDA (a marker of lipid peroxidation[89,90]), and ER stress-related proteins (Such as BiP,[91,92] p-PERK,[93,94] p-eIF2α,[95] and CHOP[96]). These results confirmed our hypothesis that the synergistic interaction between ICG and GDNPs led to ROS generation, lipid peroxidation, and ER stress. ICG acted as a trigger for ROS generation by laser irradiation, GDNPs provided a substrate for the enhancement of ER stress, and finally inhibited the growth and survival of breast tumor cells. Similar to our study, Yang Q et al found that cuprous oxide nanoparticles (CONPs) effectively triggered ER stress-induced cell apoptosis to kill renal tumor cells.[97] Liu C et al found that water-soluble Yb^{3+}, Er^{3+} codoped $NaYF_4$ nanoparticles significantly promoted human gastric adenocarcinoma cells' apoptosis by inducing mitochondrial dysfunction and ROS-mediated ER stress.[98] Li CY et al built a novel nanoformulation which utilized tumor microenvironment-responsive PEG-polyglutamic coating and dynamic charge adjustment in pancreatic tumor. This nanoformulation also triggered ER stress-induced cell apoptosis, stimulated robust ICD and exhibited effective cytotoxicity against pancreatic tumor cells.[99] Just like what Khan AA et al have reviewed,[100] many types of nanoparticles including silver, gold, silica, and graphene have been used to kill the tumor cells by inducing ER stress-mediated cell death. Mitigating ER stress in tumor cells acted by specific nanoparticles is extremely important in future treatment and understanding the action mechanism is also a good choice for the development of novel nanoplatforms.

Finally, in vivo animal experiments also showed that GDNPs@ICG substantially inhibited the growth of breast tumor, inhibited the expression of the angiogenesis marker CD31 and tumor metastasis marker N-cadherin, activated anti-tumor immune escape represented by the increased expression of IL-6, IFN-γ, and CD8, and promoted the expression of cell senescence markers, such as p16, p21, and p53. In addition, GDNPs@ICG presented limited toxic effects on blood biochemical indicators and major organs of mice, and was biocompatible. These results indicated that, in addition to inducing oxidative stress damage and ER stress, GDNPs@ICG can also enhance the photo-mediated breast tumor therapy effect by directly inhibiting breast tumor malignant behaviors.

However, our study also has some limitations. First, the tumor inhibitory effect can be further improved by adjusting the components of the GDNPs. This was because GDNPs@ICG did not reduce the tumor volume to an ideal level. Other studies have found that PTT and PDT were capable of achieving complete eradication of tumor. For instance, following a 20-day treatment regimen with a nano-photothermal DNA hydrogel (PEI@BPQDs–DNA), the tumor masses in mice were successfully eliminated.[101] A copper sulphide-based nano-platform (ADT@CuSNDs) has also been demonstrated to enable complete tumor ablation, while minimizing damage to healthy tissue to the greatest extent.[102] Furthermore, ICG has been approved for clinical use for many years, and is not a novel component used to construct bio-nanoplatform. In the future, using edible GDNPs, we may load other novel anti-tumor drugs to develop safer and more effective bio-nanoplatforms, which may have more broader clinical application prospects.

Conclusions

In conclusion, we developed a safe and controlled bio-nanoplatform (GDNPs@ICG) for efficient tumor phototherapy. The photothermal conversion efficiency of GDNPs@ICG reached 26.38%, which significantly facilitated photo-mediated breast tumor therapy. Furthermore, the combined action of GDNPs and ICG resulted in excellent tumor-killing effects through multiple mechanisms, including photothermal ablation, ROS-induced oxidative damage, lipid peroxidation, ER stress, reduced angiogenesis, inhibited metastasis, activated anti-tumor immune escape, and promotion of tumor cell senescence. Compared with synthetic nanoparticles, GDNPs possess the advantages of high yield, low immunogenicity, and a simple preparation process. Precise targeting of tumor therapy can be achieved by rational modification of the GDNPs surface groups. Hence, the GDNP-based bio-nanoplatform can be further extended to be combined with other therapeutic modalities, such as chemotherapy and immunotherapy. Moreover, GDNPs exhibit exceptional biocompatibility and stability even when converted to powder through freeze-drying, which further facilitates their potential commercial utility. In short, our study demonstrated that the novel bio-nanoplatform GDNPs@ICG substantially enhanced the photo-mediated anti-breast tumor therapy effect and could be a natural alternative for precise and efficient anti-breast tumor phototherapy.

Data Sharing Statement

These data of this manuscript can be available from the corresponding authors on reasonable request.

Ethics Approval and Informed Consent

All animal experiments were conducted in accordance with the National Institute Guide for the Care and Use of Laboratory Animals and approved by the Institutional Animal Care and Use Committee of Shengjing Hospital of China Medical University (approval number: 2024PS156K).

Acknowledgments

Thanks for the help of Dr. Xi Gu in revising this manuscript.

Author Contributions

All authors made a significant contribution to the work reported, whether in the conception, study design, execution, acquisition of data, analysis, and interpretation, or in all these areas, took part in drafting, revising, or critically reviewing the article; gave final approval of the version to be published; have agreed on the journal to which the article has been submitted; and agree to be accountable for all aspects of the work.

Funding

This work was financially supported by National Natural Science Foundation of China (81603049), Fundamental Research Funds for the Central Universities (LD2023029, DUT23YG105), Dalian Science and Technology Innovation Fund (2019J12GX045), Liaoning Provincial Science and Technology Plan Joint Plan (Applied Basic Research Project, 2023JH2/101700163), Doctoral Start-up Foundation of Liaoning Province (2023-BS-048), Application Basic Research Plan of Liaoning Province (2023JH2/101300084) and “5310” Talent Strategy Project Funding Plan of Liaoning Cancer Hospital & Institute (To Dr. Xudong Zhu).

Disclosure

The authors report no conflicts of interest in this work.

References

1. Li X, Lovell JF, Yoon J, Chen X. Clinical development and potential of photothermal and photodynamic therapies for cancer. *Nat Rev Clin Oncol*. 2020;17(11):657–674. doi:10.1038/s41571-020-0410-2
2. Shimizu K, Kahramanian A, Jabbar M, et al. Photodynamic augmentation of oncolytic virus therapy for central nervous system malignancies. *Cancer Lett*. 2023;572:216363. doi:10.1016/j.canlet.2023.216363
3. Veeranarayanan S, Mohamed MS, Poulose AC, et al. Photodynamic therapy at ultra-low NIR laser power and X-Ray imaging using Cu(3)BiS(3) nanocrystals. *Theranostics*. 2018;8(19):5231–5245. doi:10.7150/thno.25286
4. Sun Z, Zhao M, Wang W, et al. 5-ALA mediated photodynamic therapy with combined treatment improves anti-tumor efficacy of immunotherapy through boosting immunogenic cell death. *Cancer Lett*. 2023;554:216032. doi:10.1016/j.canlet.2022.216032
5. Li X, Yong T, Wei Z, et al. Reversing insufficient photothermal therapy-induced tumor relapse and metastasis by regulating cancer-associated fibroblasts. *Nat Commun*. 2022;13(1):2794. doi:10.1038/s41467-022-30306-7
6. Zhang Z, Li X, Liu W, et al. Polyphenol nanocomplex modulates lactate metabolic reprogramming and elicits immune responses to enhance cancer therapeutic effect. *Drug Resist Updat*. 2024;73:101060. doi:10.1016/j.drup.2024.101060
7. Shi F, Huang X, Hong Z, et al. Improvement strategy for immune checkpoint blockade: a focus on the combination with immunogenic cell death inducers. *Cancer Lett*. 2023;562:216167. doi:10.1016/j.canlet.2023.216167
8. Li W, Yang J, Luo L, et al. Targeting photodynamic and photothermal therapy to the endoplasmic reticulum enhances immunogenic cancer cell death. *Nat Commun*. 2019;10(1):3349. doi:10.1038/s41467-019-11269-8
9. Wang H, Li X, Tse BW, et al. Indocyanine green-incorporating nanoparticles for cancer theranostics. *Theranostics*. 2018;8(5):1227–1242. doi:10.7150/thno.22872
10. Shan W, Chen R, Zhang Q, et al. Improved Stable Indocyanine Green (ICG)-Mediated Cancer Optotheranostics with Naturalized Hepatitis B Core Particles. *Adv Mater*. 2018;30(28):e1707567. doi:10.1002/adma.201707567

11. Xiong J, Wu M, Chen J, et al. Cancer-Erythrocyte Hybrid Membrane-Camouflaged Magnetic Nanoparticles with Enhanced Photothermal-Immunotherapy for Ovarian Cancer. *ACS Nano*. 2021;15(12):19756–19770. doi:10.1021/acsnano.1c07180
12. Li Q, Chen K, Huang W, et al. Minimally invasive photothermal ablation assisted by laparoscopy as an effective preoperative neoadjuvant treatment for orthotopic hepatocellular carcinoma. *Cancer Lett*. 2021;496:169–178. doi:10.1016/j.canlet.2020.09.024
13. Yang L, Huang B, Hu S, et al. Indocyanine green assembled free oxygen-nanobubbles towards enhanced near-infrared induced photodynamic therapy. *Nano Res*. 2022;15(5):4285–4293. doi:10.1007/s12274-022-4085-0
14. Xue P, Yang R, Sun L, et al. Indocyanine Green-Conjugated Magnetic Prussian Blue Nanoparticles for Synchronous Photothermal/Photodynamic Tumor Therapy. *Nanomicro Lett*. 2018;10(4):74. doi:10.1007/s40820-018-0227-z
15. Xue P, Hou M, Sun L, et al. Calcium-carbonate packaging magnetic polydopamine nanoparticles loaded with indocyanine green for near-infrared induced photothermal/photodynamic therapy. *Acta Biomater*. 2018;81:242–255. doi:10.1016/j.actbio.2018.09.045
16. Aqil F, Gupta R. Exosomes as emerging nanoplatform in cancer therapy. *Cancer Lett*. 2023;574:216394. doi:10.1016/j.canlet.2023.216394
17. Qi R, Bai Y, Li K, et al. Cancer-associated fibroblasts suppress ferroptosis and induce gemcitabine resistance in pancreatic cancer cells by secreting exosome-derived ACSL4-targeting miRNAs. *Drug Resist Updat*. 2023;68:100960. doi:10.1016/j.drup.2023.100960
18. Mondal J, Pillarisetti S, Junnuthula V, et al. Hybrid exosomes, exosome-like nanovesicles and engineered exosomes for therapeutic applications. *J Control Release*. 2023;353:1127–1149. doi:10.1016/j.jconrel.2022.12.027
19. Li J, Feng H, Zhu J, et al. Gastric cancer derived exosomal THBS1 enhanced Vgamma9Vdelta2 T-cell function through activating RIG-I-like receptor signaling pathway in a N6-methyladenosine methylation dependent manner. *Cancer Lett*. 2023;576:216410. doi:10.1016/j.canlet.2023.216410
20. Yi Q, Xu Z, Thakur A, et al. Current understanding of plant-derived exosome-like nanoparticles in regulating the inflammatory response and immune system microenvironment. *Pharmacol Res*. 2023;190:106733. doi:10.1016/j.phrs.2023.106733
21. Kim J, Li S, Zhang S, Wang J. Plant-derived exosome-like nanoparticles and their therapeutic activities. *Asian J Pharm Sci*. 2022;17(1):53–69. doi:10.1016/j.ajps.2021.05.006
22. Mu N, Li J, Zeng L, et al. Plant-Derived Exosome-Like Nanovesicles: current Progress and Prospects. *Int J Nanomed*. 2023;18:4987–5009. doi:10.2147/IJN.S420748
23. Zhang Z, Yu Y, Zhu G, et al. The Emerging Role of Plant-Derived Exosomes-Like Nanoparticles in Immune Regulation and Periodontitis Treatment. *Front Immunol*. 2022;13:896745. doi:10.3389/fimmu.2022.896745
24. Ou X, Wang H, Tie H, et al. Novel plant-derived exosome-like nanovesicles from Catharanthus roseus: preparation, characterization, and immunostimulatory effect via TNF-alpha/NF-kappaB/PU.1 axis. *J Nanobiotechnol*. 2023;21(1):160. doi:10.1186/s12951-023-01919-x
25. Zhang M, Viennois E, Prasad M, et al. Edible ginger-derived nanoparticles: a novel therapeutic approach for the prevention and treatment of inflammatory bowel disease and colitis-associated cancer. *Biomaterials*. 2016;101:321–340. doi:10.1016/j.biomaterials.2016.06.018
26. Zhuang X, Deng ZB, Mu J, et al. Ginger-derived nanoparticles protect against alcohol-induced liver damage. *J Extracell Vesicles*. 2015;4:28713. doi:10.3402/jev.v4.28713
27. Jia Y, Li X, Meng X, Lei J, Xia Y, Yu L. Anticancer perspective of 6-shogaol: anticancer properties, mechanism of action, synergism and delivery system. *Chin Med*. 2023;18(1):138. doi:10.1186/s13020-023-00839-0
28. Kim TW, Lee HG. 6-Shogaol Overcomes Gefitinib Resistance via ER Stress in Ovarian Cancer Cells. *Int J mol Sci*. 2023;24(3):1.
29. Hu R, Zhou P, Peng YB, et al. 6-Shogaol induces apoptosis in human hepatocellular carcinoma cells and exhibits anti-tumor activity in vivo through endoplasmic reticulum stress. *PLoS One*. 2012;7(6):e39664. doi:10.1371/journal.pone.0039664
30. Yadav AK, Jang BC. Anti-Survival and Pro-Apoptotic Effects of 6-Shogaol on SW872 human Liposarcoma Cells via Control of the Intrinsic Caspase Pathway, STAT-3, AMPK, and ER Stress. *Biomolecules*. 2020;10(10):1380. doi:10.3390/biom10101380
31. Chen L, Sun K, Qin W, et al. LIMK1 m(6)A-RNA methylation recognized by YTHDC2 induces 5-FU chemoresistance in colorectal cancer via endoplasmic reticulum stress and stress granule formation. *Cancer Lett*. 2023;576:216420. doi:10.1016/j.canlet.2023.216420
32. Wang SY, Zhang LJ, Chen GJ, et al. COPA A-to-I RNA editing hijacks endoplasmic reticulum stress to promote metastasis in colorectal cancer. *Cancer Lett*. 2023;553:215995. doi:10.1016/j.canlet.2022.215995
33. Liu J, Fan L, Yu H, et al. Endoplasmic Reticulum Stress Causes Liver Cancer Cells to Release Exosomal miR-23a-3p and Up-regulate Programmed Death Ligand 1 Expression in Macrophages. *Hepatology*. 2019;70(1):241–258. doi:10.1002/hep.30607
34. Wang R, Liu Z, Fan Z, Zhan H. Lipid metabolism reprogramming of CD8(+) T cell and therapeutic implications in cancer. *Cancer Lett*. 2023;567:216267. doi:10.1016/j.canlet.2023.216267
35. Jin HR, Wang J, Wang ZJ, et al. Lipid metabolic reprogramming in tumor microenvironment: from mechanisms to therapeutics. *J Hematol Oncol*. 2023;16(1):103. doi:10.1186/s13045-023-01498-2
36. Goncalves AC, Richiardone E, Jorge J, et al. Impact of cancer metabolism on therapy resistance - Clinical implications. *Drug Resist Updat*. 2021;59:100797. doi:10.1016/j.drup.2021.100797
37. Lee S, Khoo C, Halstead CW, Huynh T, Bensoussan A. Liquid chromatographic determination of 6-, 8-, 10-gingerol, and 6-shogaol in ginger (Zingiber officinale) as the raw herb and dried aqueous extract. *J AOAC Int*. 2007;90(5):1219–1226. doi:10.1093/jaoac/90.5.1219
38. Wang W, Li CY, Wen XD, Li P, Qi LW. Simultaneous determination of 6-gingerol, 8-gingerol, 10-gingerol and 6-shogaol in rat plasma by liquid chromatography-mass spectrometry: application to pharmacokinetics. *J Chromatogr B Analyt Technol Biomed Life Sci*. 2009;877(8–9):671–-679. doi:10.1016/j.jchromb.2009.01.021
39. Lebepe TC, Oluwafemi OS. Photothermal Conversion Profiling of Large-Scaled Synthesized Gold Nanorods Using Binary Surfactant with Hydroquinone as a Reducing Agent. *Nanomaterials*. 2022;12(10):1723. doi:10.3390/nano12101723
40. Li J, Liu X, Tan L, et al. Zinc-doped Prussian blue enhances photothermal clearance of Staphylococcus aureus and promotes tissue repair in infected wounds. *Nat Commun*. 2019;10(1):4490. doi:10.1038/s41467-019-12429-6
41. Franz L, Alessandrini L, Calvanese L, Crosetta G, Frigo AC, Marioni G. Angiogenesis, programmed death ligand 1 (PD-L1) and immune microenvironment association in laryngeal carcinoma. *Pathology*. 2021;53(7):844–851. doi:10.1016/j.pathol.2021.02.007
42. Venkataramani V, Kuffer S, Cheung KCP, et al. CD31 Expression Determines Redox Status and Chemoresistance in Human Angiosarcomas. *Clin Cancer Res*. 2018;24(2):460–473. doi:10.1158/1078-0432.CCR-17-1778
43. Nadanaka S, Kinouchi H, Kitagawa H. Chondroitin sulfate-mediated N-cadherin/beta-catenin signaling is associated with basal-like breast cancer cell invasion. *J Biol Chem*. 2018;293(2):444–465. doi:10.1074/jbc.M117.814509

44. Casal JI, Bartolome RA. Beyond N-Cadherin, Relevance of Cadherins 5, 6 and 17 in Cancer Progression and Metastasis. *Int J mol Sci*. 2019;20 (13):3373. doi:10.3390/ijms20133373
45. Nguyen T, Mege RM. N-Cadherin and Fibroblast Growth Factor Receptors crosstalk in the control of developmental and cancer cell migrations. *Eur J Cell Biol*. 2016;95(11):415–426. doi:10.1016/j.ejcb.2016.05.002
46. Workenhe ST, Pol J, Kroemer G. Tumor-intrinsic determinants of immunogenic cell death modalities. *Oncoimmunology*. 2021;10(1):1893466. doi:10.1080/2162402X.2021.1893466
47. Lu Y, Xu F, Wang Y, et al. Cancer immunogenic cell death via photo-pyroptosis with light-sensitive Indoleamine 2,3-dioxygenase inhibitor conjugate. *Biomaterials*. 2021;278:121167. doi:10.1016/j.biomaterials.2021.121167
48. Rufo N, Korovesis D, Van Eygen S, et al. Stress-induced inflammation evoked by immunogenic cell death is blunted by the IRE1alpha kinase inhibitor KIRA6 through HSP60 targeting. *Cell Death Differ*. 2022;29(1):230–245. doi:10.1038/s41418-021-00853-5
49. Zhu H, He W. Ginger: a representative material of herb-derived exosome-like nanoparticles. *Front Nutr*. 2023;10:1223349. doi:10.3389/fnut.2023.1223349
50. Yan L, Cao Y, Hou L, et al. Ginger exosome-like nanoparticle-derived miRNA therapeutics: a strategic inhibitor of intestinal inflammation. *J Adv Res*. 2024. doi:10.1016/j.jare.2024.04.001
51. Sung J, Alghoul Z, Long D, Yang C, Merlin D. Oral delivery of IL-22 mRNA-loaded lipid nanoparticles targeting the injured intestinal mucosa: a novel therapeutic solution to treat ulcerative colitis. *Biomaterials*. 2022;288:121707. doi:10.1016/j.biomaterials.2022.121707
52. Qiao Z, Zhang K, Liu J, et al. Biomimetic electrodynamic nanoparticles comprising ginger-derived extracellular vesicles for synergistic anti-infective therapy. *Nat Commun*. 2022;13(1):7164. doi:10.1038/s41467-022-34883-5
53. Lai W, Yang S, Lin X, et al. Zingiber officinale: a Systematic Review of Botany, Phytochemistry and Pharmacology of Gut Microbiota-Related Gastrointestinal Benefits. *Am J Chin Med*. 2022;50(4):1007–1042. doi:10.1142/S0192415X22500410
54. Kalarikkal SP, Sundaram GM. Edible plant-derived exosomal microRNAs: exploiting a cross-kingdom regulatory mechanism for targeting SARS-CoV-2. *Toxicol Appl Pharmacol*. 2021;414:115425. doi:10.1016/j.taap.2021.115425
55. Zhang M, Wang X, Han MK, Collins JF, Merlin D. Oral administration of ginger-derived nanolipids loaded with siRNA as a novel approach for efficient siRNA drug delivery to treat ulcerative colitis. *Nanomedicine*. 2017;12(16):1927–1943. doi:10.2217/nnm-2017-0196
56. Zhang M, Xiao B, Wang H, et al. Edible Ginger-derived Nano-lipids Loaded with Doxorubicin as a Novel Drug-delivery Approach for Colon Cancer Therapy. *Mol Ther*. 2016;24(10):1783–1796. doi:10.1038/mt.2016.159
57. Wang X, Zhang M, Woloshun RR, et al. Oral Administration of Ginger-Derived Lipid Nanoparticles and Dmt1 siRNA Potentiates the Effect of Dietary Iron Restriction and Mitigates Pre-Existing Iron Overload in Hamp KO Mice. *Nutrients*. 2021;13(5):1.
58. Man F, Meng C, Liu Y, et al. The Study of Ginger-Derived Extracellular Vesicles as a Natural Nanoscale Drug Carrier and Their Intestinal Absorption in Rats. *AAPS Pharm Sci Tech*. 2021;22(6):206. doi:10.1208/s12249-021-02087-7
59. Sung J, Yang C, Collins JF, Merlin D. Preparation and Characterization of Ginger Lipid-derived Nanoparticles for Colon-targeted siRNA Delivery. *Biol Protoc*. 2020;10(14). doi:10.21769/BioProtoc.3685
60. Pei XD, He ZL, Yao HL, et al. 6-Shogaol from ginger shows anti-tumor effect in cervical carcinoma via PI3K/Akt/mTOR pathway. *Eur J Nutr*. 2021;60(5):2781–2793. doi:10.1007/s00394-020-02440-9
61. Hsu CM, Su HC, Yang MY, et al. 6-shogaol is a potential treatment for Head and Neck Squamous Cell Carcinoma. *Int J Med Sci*. 2023;20 (2):238–246. doi:10.7150/ijms.80542
62. Ajeigbe OF, Maruf OR, Anyebe DA, Opafunso IT, Ajayi BO, Farombi EO. 6- shogaol suppresses AOM/DSS-mediated colorectal adenoma through its antioxidant and anti-inflammatory effects in mice. *J Food Biochem*. 2022;46(12):e14422. doi:10.1111/jfbc.14422
63. Yang K, Dong Y, Li X, Wang F, Zhang Y. Dual-targeted delivery of paclitaxel and indocyanine green with aptamer-modified ferritin for synergetic chemo-phototherapy. *Colloids Surf B Biointerfaces*. 2023;229:113437. doi:10.1016/j.colsurfb.2023.113437
64. Shinoda K, Suganami A, Moriya Y, et al. Indocyanine green conjugated phototheranostic nanoparticle for photodiagnosis and photodynamic therapy. *Photodiagnosis Photodyn Ther*. 2022;39:103041. doi:10.1016/j.pdpdt.2022.103041
65. An Y, Chen W, Li Y, et al. Crosslinked albumin-manganese nanoaggregates with sensitized T(1) relaxivity and indocyanine green loading for multimodal imaging and cancer phototherapy. *J Mater Chem B*. 2023;11(10):2157–2165. doi:10.1039/D2TB02529A
66. Cui T, Li S, Chen S, Liang Y, Sun H, Wang L. ”Stealth” dendrimers with encapsulation of indocyanine green for photothermal and photodynamic therapy of cancer. *Int J Pharm*. 2021;600:120502. doi:10.1016/j.ijpharm.2021.120502
67. Li S, Yang S, Liu C, et al. Enhanced Photothermal-Photodynamic Therapy by Indocyanine Green and Curcumin-Loaded Layered MoS(2) Hollow Spheres via Inhibition of P-Glycoprotein. *Int J Nanomed*. 2021;16:433–442. doi:10.2147/IJN.S275938
68. Liu X, Xu N, Pu X, et al. Combined photothermal-photodynamic therapy by indocyanine green loaded polydopamine nanoparticles enhances anti-mammary gland tumor efficacy. *J Mater Chem B*. 2022;10(24):4605–4614. doi:10.1039/D2TB00565D
69. Zhang J, Zhang K, Hao Y, et al. Polydopamine nanomotors loaded indocyanine green and ferric ion for photothermal and photodynamic synergistic therapy of tumor. *J Colloid Interface Sci*. 2023;633:679–690. doi:10.1016/j.jcis.2022.11.099
70. Yan F, Wu H, Liu H, et al. Molecular imaging-guided photothermal/photodynamic therapy against tumor by iRGD-modified indocyanine green nanoparticles. *J Control Release*. 2016;224:217–228. doi:10.1016/j.jconrel.2015.12.050
71. Wang X, Zhang H, Chen X, et al. Overcoming tumor microenvironment obstacles: current approaches for boosting nanodrug delivery. *Acta Biomater*. 2023;166:42–68. doi:10.1016/j.actbio.2023.05.043
72. Shi Y, van der Meel R, Chen X, Lammers T. The EPR effect and beyond: strategies to improve tumor targeting and cancer nanomedicine treatment efficacy. *Theranostics*. 2020;10(17):7921–7924. doi:10.7150/thno.49577
73. Ikeda-Imafuku M, Wang LL, Rodrigues D, Shaha S, Zhao Z, Mitragotri S. Strategies to improve the EPR effect: a mechanistic perspective and clinical translation. *J Control Release*. 2022;345:512–536. doi:10.1016/j.jconrel.2022.03.043
74. Jeon S, Jun E, Chang H, et al. Prediction the clinical EPR effect of nanoparticles in patient-derived xenograft models. *J Control Release*. 2022;351:37–49. doi:10.1016/j.jconrel.2022.09.007
75. Knavel EM, Brace CL. Tumor ablation: common modalities and general practices. *Tech Vasc Interv Radiol*. 2013;16(4):192–200. doi:10.1053/j.tvir.2013.08.002
76. Devadasu VR, Bhardwaj V, Kumar MN. Can controversial nanotechnology promise drug delivery? *Chem Rev*. 2013;113(3):1686–1735. doi:10.1021/cr300047q

77. Csordas G, Weaver D, Hajnoczky G. Endoplasmic Reticulum-Mitochondrial Contactology: structure and Signaling Functions. *Trends Cell Biol*. 2018;28(7):523–540. doi:10.1016/j.tcb.2018.02.009
78. Murley A, Wickham K, Dillin A. Life in lockdown: orchestrating endoplasmic reticulum and lysosome homeostasis for quiescent cells. *Mol Cell*. 2022;82(19):3526–3537. doi:10.1016/j.molcel.2022.08.005
79. Chen Q, Qian Q, Xu H, et al. Mitochondrial-Targeted Metal-Phenolic Nanoparticles to Attenuate Intervertebral Disc Degeneration: alleviating Oxidative Stress and Mitochondrial Dysfunction. *ACS Nano*. 2024;18(12):8885–8905. doi:10.1021/acsnano.3c12163
80. Zeng J, Acin-Perez R, Assali EA, et al. Restoration of lysosomal acidification rescues autophagy and metabolic dysfunction in non-alcoholic fatty liver disease. *Nat Commun*. 2023;14(1):2573. doi:10.1038/s41467-023-38165-6
81. Purushothaman B, Choi J, Park S, et al. Biotin-conjugated PEGylated porphyrin self-assembled nanoparticles co-targeting mitochondria and lysosomes for advanced chemo-photodynamic combination therapy. *J Mater Chem B*. 2019;7(1):65–79. doi:10.1039/C8TB01923A
82. Wang B, Wang Y, Zhang J, et al. ROS-induced lipid peroxidation modulates cell death outcome: mechanisms behind apoptosis, autophagy, and ferroptosis. *Arch Toxicol*. 2023;97(6):1439–1451. doi:10.1007/s00204-023-03476-6
83. Su LJ, Zhang JH, Gomez H, et al. Reactive oxygen species-induced lipid peroxidation in apoptosis, autophagy, and ferroptosis. *Oxid Med Cell Longev*. 2019;2019:5080843. doi:10.1155/2019/5080843
84. Xie Z, Hou H, Luo D, An R, Zhao Y, Qiu C. ROS-dependent lipid peroxidation and reliant antioxidant ferroptosis-suppressor-protein 1 in rheumatoid arthritis: a covert clue for potential therapy. *Inflammation*. 2021;44(1):35–47. doi:10.1007/s10753-020-01338-2
85. Celik C, Lee SYT, Yap WS, Thibault G. Endoplasmic reticulum stress and lipids in health and diseases. *Prog Lipid Res*. 2023;89:101198. doi:10.1016/j.plipres.2022.101198
86. Guillen-Samander A, De Camilli P. Endoplasmic reticulum membrane contact sites, lipid transport, and neurodegeneration. *Cold Spring Harb Perspect Biol*. 2023;15(4):a041257. doi:10.1101/cshperspect.a041257
87. Cybulsky AV. Endoplasmic reticulum stress, the unfolded protein response and autophagy in kidney diseases. *Nat Rev Nephrol*. 2017;13(11):681–696. doi:10.1038/nrneph.2017.129
88. Wiseman RL, Mesgarzadeh JS, Hendershot LM. Reshaping endoplasmic reticulum quality control through the unfolded protein response. *Mol Cell*. 2022;82(8):1477–1491. doi:10.1016/j.molcel.2022.03.025
89. Tsikas D. Assessment of lipid peroxidation by measuring malondialdehyde (MDA) and relatives in biological samples: analytical and biological challenges. *Anal Biochem*. 2017;524:13–30. doi:10.1016/j.ab.2016.10.021
90. Nguyen TT, Ngo LQ, Promsudthi A, Surarit R. Salivary lipid peroxidation in patients with generalized chronic periodontitis and acute coronary syndrome. *J Periodontol*. 2016;87(2):134–141. doi:10.1902/jop.2015.150353
91. Liu Z, Liu G, Ha DP, Wang J, Xiong M, Lee AS. ER chaperone GRP78/BiP translocates to the nucleus under stress and acts as a transcriptional regulator. *Proc Natl Acad Sci U S A*. 2023;120(31):e2303448120. doi:10.1073/pnas.2303448120
92. She C, Wu C, Guo W, et al. Combination of RUNX1 inhibitor and gemcitabine mitigates chemo-resistance in pancreatic ductal adenocarcinoma by modulating BiP/PERK/eIF2alpha-axis-mediated endoplasmic reticulum stress. *J Exp Clin Cancer Res*. 2023;42(1):238. doi:10.1186/s13046-023-02814-x
93. Balsa E, Soustek MS, Thomas A, et al. ER and nutrient stress promote assembly of respiratory chain supercomplexes through the PERK-eIF2alpha axis. *Mol Cell*. 2019;74(5):877–890e876. doi:10.1016/j.molcel.2019.03.031
94. Narayanan S, Elesela S, Rasky AJ, et al. ER stress protein PERK promotes inappropriate innate immune responses and pathogenesis during RSV infection. *J Leukoc Biol*. 2022;111(2):379–389. doi:10.1002/JLB.3A0520-322RR
95. Dang TT, Kim MJ, Lee YY, et al. Phosphorylation of EIF2S1 (eukaryotic translation initiation factor 2 subunit alpha) is indispensable for nuclear translocation of TFEB and TFE3 during ER stress. *Autophagy*. 2023;19(7):2111–2142. doi:10.1080/15548627.2023.2173900
96. Hu H, Tian M, Ding C, Yu S. The C/EBP homologous protein (CHOP) transcription factor functions in endoplasmic reticulum stress-induced apoptosis and microbial infection. *Front Immunol*. 2018;9:3083. doi:10.3389/fimmu.2018.03083
97. Yang Q, Wang Y, Yang Q, et al. Cuprous oxide nanoparticles trigger ER stress-induced apoptosis by regulating copper trafficking and overcoming resistance to sunitinib therapy in renal cancer. *Biomaterials*. 2017;146:72–85. doi:10.1016/j.biomaterials.2017.09.008
98. Liu C, Sun S, Mao J. Water-soluble Yb(3+), Er(3+) codoped NaYF(4) nanoparticles induced SGC-7901 cell apoptosis through mitochondrial dysfunction and ROS-mediated ER stress. *Hum Exp Toxicol*. 2023;42:9603271231188493. doi:10.1177/09603271231188493
99. Li CY, Chou TF, Lo YL. An innovative nanoformulation utilizing tumor microenvironment-responsive PEG-polyglutamic coating and dynamic charge adjustment for specific targeting of ER stress inducer, microRNA, and immunoadjuvant in pancreatic cancer: in vitro investigations. *Int J Biol Macromol*. 2024;254(Pt 2):127905. doi:10.1016/j.ijbiomac.2023.127905
100. Khan AA, Allemailem KS, Almatroudi A, et al. Endoplasmic reticulum stress provocation by different nanoparticles: an innovative approach to manage the cancer and other common diseases. *Molecules*. 2020;25(22):5336. doi:10.3390/molecules25225336
101. Zhou L, Pi W, Hao M, et al. An injectable and biodegradable nano-photothermal DNA hydrogel enhances penetration and efficacy of tumor therapy. *Biomater Sci*. 2021;9(14):4904–4921. doi:10.1039/D1BM00568E
102. Cheng J, Zhu Y, Dai Y, et al. Gas-mediated tumor energy remodeling for sensitizing mild photothermal therapy. *Angew Chem Int Ed Engl*. 2023;62(27):e202304312. doi:10.1002/anie.202304312